

# Rockwall permafrost dynamics evidenced by Repeated and Automated Electrical Resistivity Tomography at Aiguille du Midi (3842 m a.s.l., French Alps)

Feras Abdulsamad<sup>1,2</sup>, Josué Bock<sup>1</sup>, Florence Magnin<sup>1</sup>, Emmanuel Malet<sup>1</sup>, André Revil<sup>1</sup>,  
Matan Ben-Asher<sup>1</sup>, Jessy Richard<sup>1,2</sup>, Pierre-Allain Duvillard<sup>2</sup>, Marios Karaoulis<sup>3</sup>, Thomas  
Condom<sup>4</sup>, Ludovic Ravanel<sup>1</sup> and Philip Deline<sup>1</sup>

1. EDYTEM, CNRS - Université Savoie Mont-Blanc, 73370 Le Bourget du Lac, France

2. Naga Geophysics, 229 rue Joseph Fontanet 73000 Chambéry, France

3. School of Geology, Geophysics Department, Aristotle University of Thessaloniki, Thessaloniki, Greece

4. Univ. Grenoble Alpes, IRD, CNRS, INRAE, Grenoble-INP, IGE, 38000 Grenoble, France

**Corresponding author:** Abdulsamad Feras (feras.abdul-samad@univ-smb.fr)

**Emails:** [feras.abdul-samad@naga-geophysics.com](mailto:feras.abdul-samad@naga-geophysics.com); [andre.revil@univ-smb.fr](mailto:andre.revil@univ-smb.fr);  
[ludovic.ravanel@univ-smb.fr](mailto:ludovic.ravanel@univ-smb.fr); [florence.magnin@univ-smb.fr](mailto:florence.magnin@univ-smb.fr); [mkaraoulis@geo.auth.gr](mailto:mkaraoulis@geo.auth.gr);  
[matan.ben-asher@univ-smb.fr](mailto:matan.ben-asher@univ-smb.fr); [pierre-allain.duvillard@naga-geophysics.com](mailto:pierre-allain.duvillard@naga-geophysics.com);  
[josue.bock@laposte.net](mailto:josue.bock@laposte.net); [emmanuel.malet@univ-savoie.fr](mailto:emmanuel.malet@univ-savoie.fr); [jessy.richard@naga-geophysics.com](mailto:jessy.richard@naga-geophysics.com);  
[thomas.condom@ird.fr](mailto:thomas.condom@ird.fr); [philip.deline@univ-smb.fr](mailto:philip.deline@univ-smb.fr)

**Keywords:** Rockwall permafrost dynamics; Active layer thickness; Electrical resistivity  
tomography; Temperature measurements.

*Intended for publication in The Cryosphere*

26 **Abstract.** Permafrost degradation significantly affects the stability of rockwalls in high altitude  
27 regions. Monitoring rockwall permafrost is essential for assessing potential geohazards. While  
28 borehole temperature measurements are the most direct permafrost monitoring approach, they  
29 lack sufficient spatial representation in such highly heterogeneous ground conditions.  
30 Conversely, geoelectrical measurements can provide more comprehensive insights into these  
31 complex patterns and dynamics. This study investigates the permafrost dynamics and intends  
32 to detect potential hydrogeological processes at the Aiguille du Midi (3842 m a.s.l., French  
33 Alps) using repeated and Automated-Electrical Resistivity Tomography (A-ERT) approaches,  
34 covering a period of 3.5 years (06/2020-12/2023). A total of three geoelectrical profiles have  
35 been installed on three faces of the Aiguille du Midi (N-W, S and E). An automated acquisition  
36 system for permanent resistivity monitoring and remote data acquisition is implemented. A  
37 time-lapse inversion technique is employed to get the temporal and spatial variations of  
38 electrical resistivity at seasonal and interannual time scales. The data revealed significant  
39 variations in active layer thickness across rock faces, along with a slight decrease in electrical  
40 resistivity at depth, indicating permafrost warming over time. However, they did not provide  
41 clear evidence of water pressurization in rock fractures. Using a petrophysical model, calibrated  
42 with laboratory measurements of the temperature dependence of electrical resistivity of granite  
43 sample, we estimated the temperature within the frozen zone from the resistivity measurements,  
44 under favorable condition at surface in summer and autumn. Validation against direct  
45 temperature measurements in a 10-m depth borehole along the NW profile indicates a mean  
46 absolute error less than 1 °C within the frozen zone. This research underscores the efficacy of  
47 ERT as a promising, non-invasive tool for quantitative monitoring of permafrost dynamics in  
48 Alpine environments. It also reveals challenges associated with conducting A-ERT in high  
49 mountain rockwalls where the contact resistance is very high (~500 k $\Omega$ ) and sometimes  
50 intermittent due to factors such as thunder strikes and rockfalls.

## 51 **1. Introduction**

52 Climate change accelerates the degradation of the permafrost in high-mountains areas  
53 worldwide (Smith et al., 2022). In the European Alps, permafrost has warmed up to  $> 1^{\circ}\text{C}$  at  
54 10 m depth, especially in bedrock permafrost (Etzelmüller et al., 2020; Magnin et al., 2024;  
55 Noetzli et al., 2024). Over the last decade, there has been a continuous increase in rockfall  
56 events, particularly those impacting permafrost in the European Alps (Cathala et al., 2024;  
57 Jacquemart et al., 2024; Ravanel et al., 2017). Infrastructure located in high altitude are  
58 increasingly affected by these events (Duvillard et al., 2021, 2018; Hartmeyer et al. 2020).  
59 Permafrost degradation of the rock mass can also locally be accelerated by heat advection  
60 through water infiltration in fractures (see for example Hasler et al., (2011) for a laboratory  
61 experiment; Magnin and Josnin (2021) for a numerical experiment), leading to erosion of the  
62 ice-infill (Hauck and Hilbich, 2024; Hartmeyer et al. 2020). As a result, a loss of bonding  
63 between rock and ice may occur, which in turn alters the mechanical properties of such  
64 assemblage (Mamot et al., 2018; Krautblatter et al., 2013). Therefore, understanding the  
65 thermo-hydrogeological dynamics of steep Alpine rock faces is essential for assessing potential  
66 geohazards associated with permafrost degradation.

67 To assess permafrost warming, one approach is to directly determine and monitor  
68 rockwall temperatures using temperature sensors installed at the rock surface or in boreholes  
69 (*e.g.*, Magnin et al., 2024). Although borehole temperature monitoring is still the only direct  
70 method to detect and monitor permafrost, it provides only point-scale information, while its  
71 distribution and evolution can be highly variable in extreme topographical conditions. In  
72 addition, boreholes in rockwall at high altitude are logistically difficult to realize. and are also  
73 expensive and invasive.

74 On the other hand, geophysical measurements provide higher spatial coverage with  
75 respect to boreholes. Various non- or minimally intrusive methods have been applied to

76 evaluate permafrost, including Refraction Seismic Tomography (RST) (*e.g.*, Steiner et al.,  
77 2019; Draebing 2016), Ground Penetrating Radar (GPR) (Campbell et al., 2018), Electrical  
78 Resistivity Tomography (ERT) (*e.g.*, Mollaret et al., 2020; Krautblatter and Hauck 2007) and  
79 Induced Polarization (IP) (Maierhofer et al., 2024; Abdulsamad et al., 2019; Duvillard et al.,  
80 2018; Doetsch et al., 2015). Combined geophysical methods can take advantage of the  
81 complementary petrophysical and spatial sensitivities of these different methods. For instance,  
82 ERT measurement was combined with RST to evaluate ice, air, water, and rock contents  
83 (Mewes et al., 2017; Hauck et al., 2011). Recently, joint inversion of ERT and RST could  
84 reduce the uncertainties in the evaluation of air, water, ice and rock contents (Pavoni et al.,  
85 2023; Steiner et al., 2021; Mollaret et al., 2020; Wagner et al., 2019). IP measurements  
86 (providing tomograms of the electrical conductivity and normalized chargeability) have been  
87 recently used to assess the distribution of permafrost temperature, relying on laboratory  
88 calibration and a petrophysical (physics-based) model connecting resistivity and normalized  
89 chargeability with temperature under frozen and unfrozen conditions (see Moser et al., 2025;  
90 Duvillard et al., 2021, 2018; Revil et al. 2026a, b and references therein).

91 In the last two decades, ERT has become an increasingly popular tool in permafrost  
92 studies (*e.g.*, Herring et al., 2023; Farzamain et al., 2020; Magnin et al., 2015a; Krautblatter et  
93 al., 2010). Herring et al. (2023) provide a review of the use of ERT method in permafrost  
94 research, detailing both the advantages and limitations of this method in such a context. A  
95 significant advantage of using electrical resistivity measurements to assess mountain  
96 permafrost is that the freezing and thawing of water filling pores are associated with  
97 considerable changes in resistivity (generally between one to three orders of magnitude, see  
98 Coperey et al., 2019). Because of this sensitivity, electrical resistivity tomograms can be used  
99 to assess the presence and distribution of permafrost.

100 Repeated ERT measurements at specific time intervals using the same survey geometry  
101 can be used to track the temporal and spatial evolution of permafrost over time (*e.g.*, Offer et  
102 al., 2025, Hilbich et al., 2008). However, rapid changes due to water flow, infiltration or  
103 drainage (such as during snowmelt or rainfall) may not be captured by monthly or seasonally  
104 repeated measurements (Krautblatter et al., 2010). Alternatively, continuous resistivity  
105 measurements, known as Automated-ERT (A-ERT) or ERT monitoring, offer the ability to  
106 track the ongoing evolution of permafrost and capture rapid, heterogeneous and non-linear  
107 changes in its temperature and ice content (*e.g.*, Scandroglia et al., 2021; Doetsch et al., 2015).  
108 A-ERT over period of several years has been recently used to track the degradation of  
109 permafrost associated with global warming (Mollaret et al., 2019; Keusching et al., 2017;  
110 Doetsch et al., 2015; Hilbich et al., 2008).

111 Furthermore, the time-lapse inversion of geophysical data derived from a fixed  
112 monitoring network provides a succession of tomograms showing the spatial and temporal  
113 changes in subsurface resistivity (see; Karaoulis et al., 2013; Loke, 1999). The results of time-  
114 lapse inversions of apparent resistivity data can be directly linked to the evolution of permafrost  
115 throughout the annual cycle or to rapid variations caused by water infiltration or drainage during  
116 short periods of time (Cimpoiasu et al., 2025; Keusching et al., 2017; Hilbich et al., 2008).

117 That said, A-ERT at high altitudes (>3500 m) and over a multi-profile setting has not  
118 yet been tested for pluriannual permafrost monitoring. The use of A-ERT under high-altitude  
119 conditions presents specific challenges due to extreme topographical and climatic conditions as  
120 well as meteorological events. However, it could provide valuable information about the  
121 hydrogeological system and the evolution of permafrost in environments where its distribution  
122 and dynamic are highly heterogeneous.

123 In this study, we present the results of an A-ERT survey conducted over nearly four  
124 years (2020-2023) at Aiguille du Midi (AdM) in the Mont-Blanc massif (French Alps). The site

125 consists of massive and fractured granite and includes infrastructure such as tunnels and  
126 elevators. Water infiltration was observed at various locations within the tunnels. The objective  
127 of this study is to investigate permafrost dynamics from infra-seasonal to multiyear timescales  
128 and through various rock faces of the same site. Our goals are: (1) evaluating the potential of  
129 A-ERT to characterize seasonal to pluriannual permafrost dynamics, their heterogeneity and  
130 non-linearity in steep alpine rockwalls; (2) assessing the accuracy of temperature derived from  
131 resistivity measurements; and (3) attempting to detect potential water circulation pathways in  
132 fractures, along with their thermal impacts. For this objective, a total of three ERT profiles were  
133 deployed downwards from the summit in three directions: North-West (NW), South (S) and  
134 East (E). Each profile consists of 32 electrodes spaced at 5 m. In addition to field data,  
135 laboratory resistivity measurements were conducted on granite core samples, in both unfrozen  
136 and frozen conditions. Furthermore, temperature was continuously monitored in a 10 m-deep  
137 borehole along the NW profile and was used to quantitatively evaluate the accuracy of  
138 temperature estimates derived from geophysical measurements of electrical resistivity.

## 139 **2. Study site**

140 We investigate the Aiguille du Midi (3842 m a.s.l.), which is the highest and most  
141 western summit of the Aiguilles de Chamonix (Fig. 1a). It is located on the NW flank of the  
142 Mont-Blanc massif. It includes three peaks that are all connected by human-made bridges and  
143 galleries and hosts major touristic and technical infrastructures. During the summer season,  
144 AdM is visited by approximately 5000 visitors per day, who are transported from the city of  
145 Chamonix by cable car, making it one of the most intensively frequented high-alpine sites in  
146 the European Alps. Since the 1950s, the morphology and appearance of the summit have been  
147 strongly modified by construction and infrastructure development (Fig. 1). These factors,  
148 combined with the extreme topography characterized by near-vertical rock walls with an  
149 average slope of  $78^\circ$  on the northwestern face, make the site particularly prone to rock

150 instability processes. Consequently, AdM represents a critical location where geotechnical and  
151 geophysical monitoring is essential to ensure the long-term stability of the infrastructures and  
152 the safety of visitors. Our study focuses on the central peak, which is the highest among the  
153 three, and which hosts the cable-car station connecting AdM to Pointe Helbronner with the  
154 *Panoramic Mont-Blanc* cable car.

155 The lithology in the study area is dominated by massive granite with a very low porosity  
156 ( $\sim 0.01$ , Magnin et al., 2015a). The highest parts (3740 to 3840 m a.s.l.) of the peak tend to be  
157 steep, contain few large fractures, and, in places, are characterized by vertical foliation bands  
158 and small cracks (Magnin et al., 2015b). Figure 2 shows the mean monthly and annual air  
159 temperature at AdM during the study period. The year 2021 was the coolest year (yearly  
160 averages:  $-5.8\text{ }^{\circ}\text{C}$ ,  $-6.9\text{ }^{\circ}\text{C}$ ,  $-5.3\text{ }^{\circ}\text{C}$ , and  $-5.7\text{ }^{\circ}\text{C}$  from 2020 to 2023, respectively), and 2022 was  
161 the warmest especially due to extremely warm summer that had important consequences on  
162 rock temperature (Magnin et al., 2024; Bruel et al., 2026).

163 In order to evaluate the thermal state and the distribution of permafrost at AdM, three  
164 boreholes have been drilled in 2009. They are labeled BH-NW on the NW face, BH-S on the  
165 South face and BH-E on the East face. Each borehole is 10-m-deep and 66 mm in diameter and  
166 was drilled normal to the topography (their position is shown in Fig. 1b-d). Each borehole is  
167 equipped with 15-thermistor strings calibrated in an ice-water bath and then placed at different  
168 depths in the borehole. Figure A1 shows the temperature measured in BH-NW and BH-S at  
169 different dates.

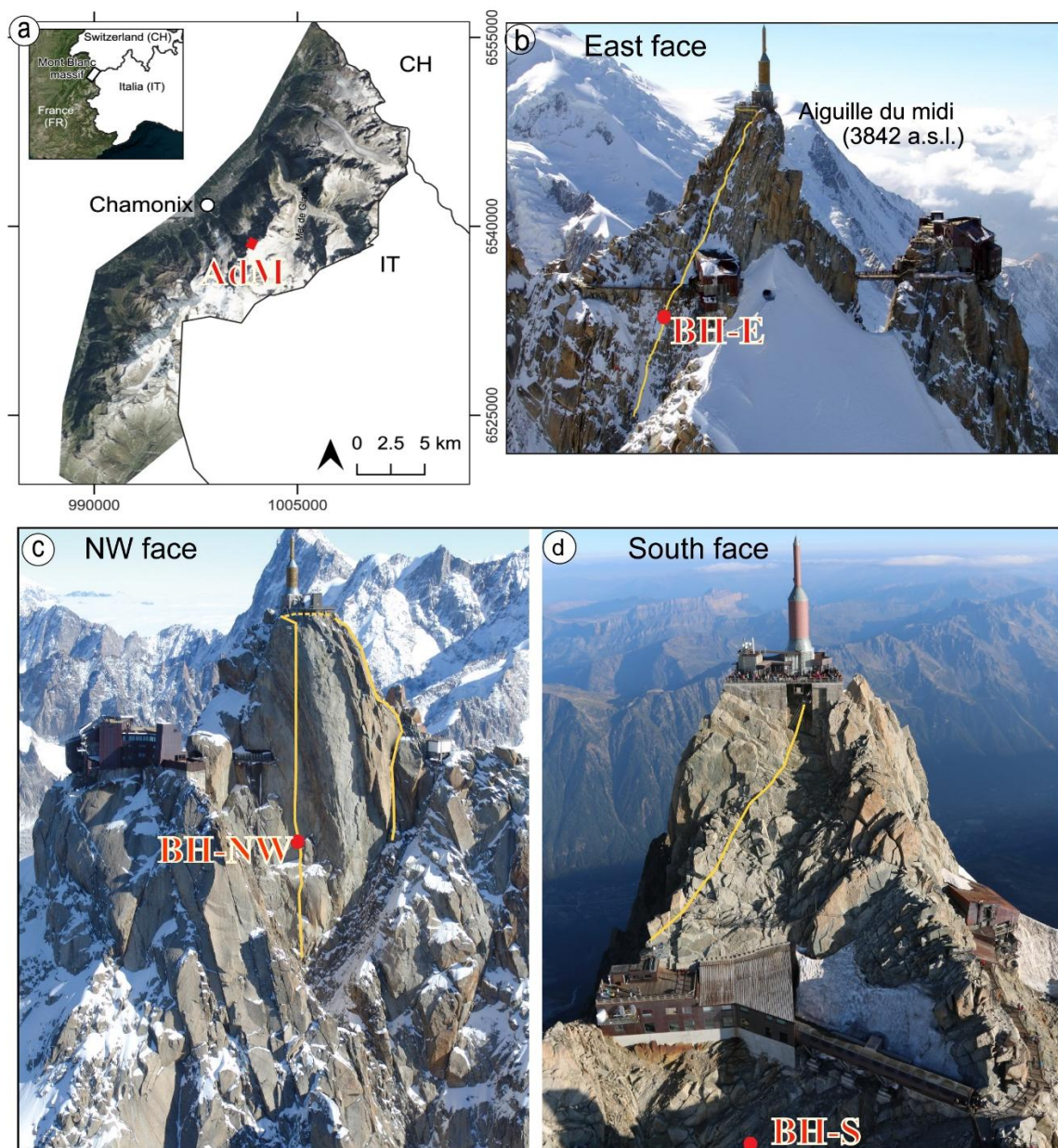
170 The temperature of the permafrost core shows significant variability between the South  
171 and North-West faces of the AdM. For example, at a depth of 10 meters, the temperature is  
172 approximately  $-4\text{ }^{\circ}\text{C}$  on the NW face, while it is around  $-1\text{ }^{\circ}\text{C}$  on the sun-exposed S face  
173 (Magnin et al., 2024). These temperature differences indicate the presence of strong  
174 temperature gradients within the rock mass. In the same way, the Active Layer Thickness (ALT,

175 *i.e.*, the maximum seasonal thaw layer) is also highly variable as interpolated between  
176 temperature sensors: it is observed to be around 1.3 to 2.7 m in summer on the NW side, while  
177 it reaches 4.8 to 7.6 m on the S side in the early fall. Below this depth, permafrost is present  
178 (Magnin et al., 2024). Figure A1 (appendix A) shows the temperature variation over depth in  
179 boreholes BH-NW and BH-S on different dates

180         BH-NW is located along an electrical resistivity profile (NW profile) and is positioned  
181 between electrodes 8 and 9 (counted from the bottom) of the NW profile (see Fig. 1c). The  
182 temperature measured in this borehole is used to assess the accuracy of the temperature derived  
183 from ERT results using the petrophysical model presented in the next section.

184

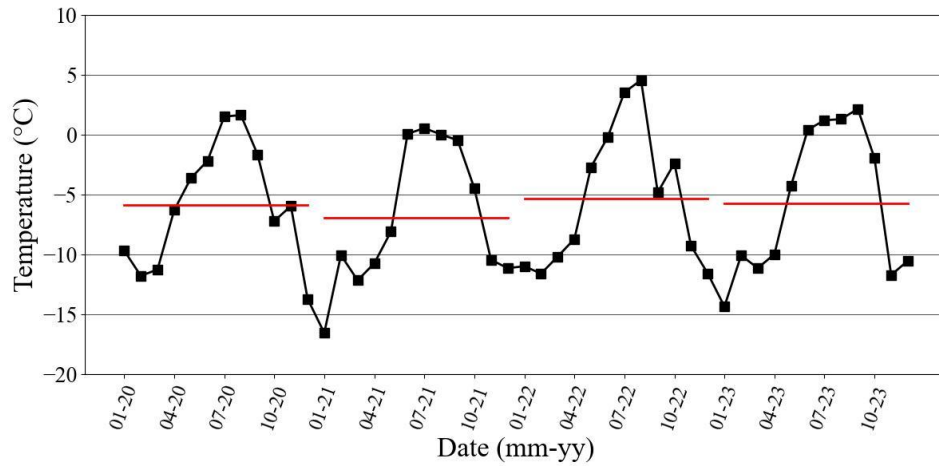
185



186

187 **Figure 1.** Study site location and geophysical survey setting. The yellow lines indicate the approximate  
 188 positions of electrical resistivity profiles on each side (NW, E and S profiles). The red dots denote the  
 189 borehole locations. (a) Location of the study site (Aiguille du Midi (AdM)), in the Mont Blanc massif  
 190 (here, the French side). The electrical resistivity profile and borehole locations at the East face(b), at the  
 191 North-West face (c) and at the South face (d).

192



193

194 **Figure 2.** Monthly average air temperature (°C) at AdM during the survey period (Data from the  
 195 meteorological station of Institute of Environmental Geosciences at the Aiguille du Midi). Horizontal  
 196 bars show the annual average air temperature.

197

### 198 3. Electrical conductivity - temperature relationship

199 The electrical conductivity of a rock represents its ability to conduct an electrical current  
 200 under the application of an imposed electrical field. The electrical conductivity (inverse of the  
 201 electrical resistivity) of a rock depends on its porosity  $\phi$  (dimensionless), water content  $\theta$   
 202 (dimensionless), pore water conductivity, Cation Exchange Capacity (CEC), and rock  
 203 temperature  $T$  (in °C) (*e.g.*, Revil et al., 1998).

204 Above the freezing point (typically, but not necessary, around 0°C), electrical  
 205 conductivity ( $\sigma(T)$  in  $\text{S m}^{-1}$ ) increases linearly with temperature according to Revil et al. (1998):

$$206 \quad \sigma(T) = \sigma(T_0)[1 + \alpha_T(T - T_0)], \quad (1)$$

207 where  $\alpha_T = 0.021 \pm 0.02 \text{ } ^\circ\text{C}^{-1}$ ,  $T_0 = 25^\circ\text{C}$  denotes the reference temperature, and  $\sigma(T_0)$  denotes  
 208 the conductivity of the rock at the reference temperature. Equation (1) results from the effect of  
 209 temperature on the mobility of the ions in the pore water and in the electrical double layer  
 210 coating the surface of the grains.

211 In contrast, under freezing conditions, temperature variations have a significant  
 212 influence on electrical conductivity because of the occurrence of an insulating phase (*i.e.*, ice  
 213 formation) in the pore space and despite the increase in the salinity of the pore water with  
 214 temperature decrease. This temperature dependence of electrical conductivity can be modeled  
 215 as follows (see details in Duvillard et al., 2018; 2021; Coperey et al., 2019):

$$216 \quad \sigma(T) \approx \left[ (\phi - \theta_r) \exp\left(-\frac{T - T_F}{T_C}\right) + \theta_r \right] \frac{\sigma(T_0)}{\phi} [1 + \alpha_T (T - T_0)], \quad (2)$$

217 where  $\theta_r$  (dimensionless) denotes the residual water content when  $T \ll T_F$ ,  $T_F$  denotes the  
 218 liquidus or freezing point/temperature,  $T_C$  denotes a characteristic temperature controlling the  
 219 transition between the unfrozen state and the frozen state, and  $\phi - \theta_r$  denotes the maximum  
 220 volumetric ice content at low temperatures. Equation (2) provides the opportunity to convert  
 221 electrical conductivity or electrical resistivity tomogram measured in the field to a temperature  
 222 distribution (*e.g.*, Duvillard et al., 2021).

223

## 224 4. Methods

### 225 4.1 Laboratory measurements

226 In order to calibrate our field measurements and evaluate the parameters (*e.g.*,  $T_C$ ,  $\theta_r$ )  
 227 in the petrophysical model discussed above (Section 3), we conducted an electrical conductivity  
 228 experiment on a granite rock sample collected from an outcrop at the study site. The cube-  
 229 shaped granite sample (dimensions:  $5 \times 5 \times 5 \text{ cm}^3$ ) was dried during 24 h at approximately 100  
 230 °C, then saturated under vacuum with degassed water. The saturated water conductivity was  
 231  $0.016 \text{ S m}^{-1}$  at equilibrium at  $T = 25^\circ\text{C}$ . This value is representative of the conductivity of  
 232 infiltrating water collected and measured in galleries at the AdM site (approximately  $150 \mu\text{S/cm}$   
 233 or  $0.015 \text{ S m}^{-1}$ , see Ben-Asher et al. (2026). The sample was left in the solution for several

234 weeks to reach chemical equilibrium before performing the laboratory measurements. The  
235 sample was characterized by a very low measured porosity  $\phi = 0.014$ .

236 For thermal-resistivity analysis, the sample was placed in a heat-resistant insulating bag  
237 immersed in a thermostat bath (KISS K6 from Huber; dimensions: 210×400×546 mm<sup>3</sup>; bath  
238 volume: 4.5 L). The temperature of the bath was controlled with a precision of 0.1 °C. Glycol  
239 was used as the heat carrying fluid (Coperey et al., 2019). Thin Carbon film electrodes were  
240 used for both current injections and potential measurement. The complex conductivity spectra  
241 were obtained over the temperature range of +10 to -10 °C, using a high-precision impedance-  
242 meter ZEL-SIP04-V02 (Zimmermann et al., 2008). The resistivity measurements reported here  
243 are at a frequency of 1 Hz (Coperey et al., 2019).

244

#### 245 **4.2 ERT Data acquisition**

246 ERT has been conducted over a four-years period (06/2020 - 12/2023). A total of three  
247 cables, each with 32 take-outs spaced 5 m (for a profile length of 155 m), were installed. The  
248 three cables were deployed downwards from the summit in three directions: North-West (NW),  
249 East (E) and South (S). The S profile starts at the South side and passes to the North-West side  
250 around mid-distance (see Fig. 1c, d). The cables were installed gradually (over a year) starting  
251 from NW side (installed in June 2020), then on the South side (installed in July and August  
252 2020), and finally on the East side (installation finished in March 2021 because of snowpack in  
253 2020 at this side). In order to ensure good electrical contact between electrodes and rock mass,  
254 stainless steel (A4/316) climbing bolts (Fischer 10×126 mm) poured in salty bentonite were  
255 used and placed firmly in holes drilled in the rock. A specially designed jumper was used to  
256 attach each take-out to the bolt to ensure maximum contact. The resistivity cables were attached  
257 to anchors to minimize damage from rockfall and snow pressure.

258 A LS2-Terrameter (ABEM) with internal impedance of 20 M $\Omega$  was used for the data  
259 acquisition. The ERT device and control system for monitoring were deployed inside the  
260 summit station with network access, power connection, and overvoltage protection. Data  
261 acquisition was fully automated and remotely controlled since September 2021. Finally, the  
262 position of every electrode was measured using a differential GPS when the signal is available  
263 and a theodolite in steep areas. The measurements were carried out using a Wenner  
264 configuration, which provides a high signal-to-noise ratio and is widely used in mountain  
265 permafrost environments (Mollaret et al., 2020; Krautblatter and Hauck, 2007; Dahlin and  
266 Zhou, 2004). Each profile consists of 155 data points. An injected current ranging from 0.1 mA  
267 to 200 mA was applied, with a maximum stack number of 4 was applied to ensure a standard  
268 deviation of less than 5 % in the measured resistivity. The first measurements were performed  
269 in June 2020. Between June 2020 and September 2021, ERT measurements were repeated  
270 occasionally. Then the continuous measurements started in late September 2021 after  
271 developing an automated system of acquisition. Datasets were daily recorded for each profile  
272 (NW, S and E profiles).

273 A Contact Resistance (CR) test was performed before each series of measurements. A  
274 high contact resistance in the rock wall (>100 k $\Omega$ ) was encountered throughout the entire survey  
275 period, which posed a challenge to the quality and continuity of data acquisition. CR varies  
276 between a few k $\Omega$  and 10 000 k $\Omega$ . However, beyond a CR threshold, the ERT measurements  
277 lose their accuracy. Electrodes with high CR (>600 k $\Omega$ ) are excluded automatically by the LS2,  
278 leading to gaps in the pseudo-section of apparent resistivity. Special efforts were made to reduce  
279 CR and improve the electrode/rock contact, including the addition of salty water, using copper  
280 electrodes and duplicate electrodes. The latter one resulted in a significant and durable  
281 improvement in CR (one order of magnitude reduction in CR). Figure B1 shows the temporal  
282 evolution of CR at profiles S and NW, as well as gaps in the A-ERT measurements caused by

283 cable defects. It also indicates the date of duplicate electrode installation, highlighting a  
284 reduction in contact resistance following installation.

285 The A-ERT ran into numerous software and hardware issues, resulting in unsystematic  
286 data gaps. The E face cable was severely damaged by a lightning strike, before being destroyed  
287 by an uncontrolled rock purge. Additionally, NW and S cables were both damaged by rockfalls,  
288 leading to significant data gaps (see Fig. 3 and Fig. B1). Repairing or replacing the damaged  
289 cables was not possible for several reasons (e.g., limited access to the cable path because of  
290 accumulated snowpack). Data acquisition on the Eastern side (E profile) encountered numerous  
291 challenges related to contact resistance, rockfalls and cable connections, resulting in long gaps  
292 and insufficient data for long time analysis or time-lapse inversion.

293

### 294 **4.3. Data processing and inversion**

295 The apparent resistivities were calculated using the open-source package pyGIMLi  
296 (Rücker et al., 2017), which combines measured resistances and electrode positions.

297

298 For datasets used in inversion, a systematic quality-control procedure was applied prior  
299 to processing. The primary selection criterion was the number of connected electrodes within  
300 each pseudo-section. Up to four unconnected electrodes (typically due to high contact  
301 resistance) were tolerated, depending on their positions, since electrode contributions are not  
302 equal in the pseudo-section. After selecting valid datasets, outlier removal was performed. To  
303 define appropriate filtering threshold, we individually analyzed representative pseudo-sections  
304 acquired in autumn and spring (completed datasets). As a result of this analysis, we filtered  
305 outliers out of the range (300  $\Omega\text{m}$  - 20 k $\Omega\text{m}$ ) for data measured in summer and autumn, and out  
306 of range (300  $\Omega\text{m}$  - 200 k $\Omega\text{m}$ ) for data measured in spring and winter. Table C1 (appendix C)  
307 summarizes the data presented in this study. In most cases, more than 80 % of the originally  
308 recorded data points were retained in each pseudo-section after filtering.

309           The inversion of the electrical resistivity datasets was performed using the open-source  
310 package pyGIMLi (Rücker et al., 2017; Günther et al., 2006). The inversion uses a Gauss-  
311 Newton minimization algorithm of a cost-function penalizing the roughness of the electrical  
312 resistivity distribution on an irregular grid (Günther et al., 2006). In the absence of a reciprocal  
313 dataset to estimate errors in measurements, we used a linear error model which assumed 5 %  
314 relative error and absolute error  $1e-5$ . The parameters used in the inversion process are  $zWeight$   
315 = 10 and smoothness ( $\lambda$ ) equal one. The inversion parameter  $zWeight$  is chosen higher  
316 than one to enhance the vertical discontinuities and vertical structures (*i.e.*, to better delineate  
317 the active layer and infrastructures), during the inversion process. Following Mollaret et al.  
318 (2020), an iterative process was conducted to select the smoothness parameter ( $\lambda$ ) that  
319 minimizes the data misfit of individual inversions of a reference dataset (dataset of 30/06/2020).  
320 The root-mean-square (RMS) error is evaluated at the end of each inversion and reported at the  
321 figures. In order to track the seasonal and interannual variations in the permafrost, a time-lapse  
322 inversion approach was employed. In this case, the reference model was moved along with the  
323 inversion so that the difference to the preceding step is constrained (Doetsch et al., 2015;  
324 Karaoulis et al., 2013).

325

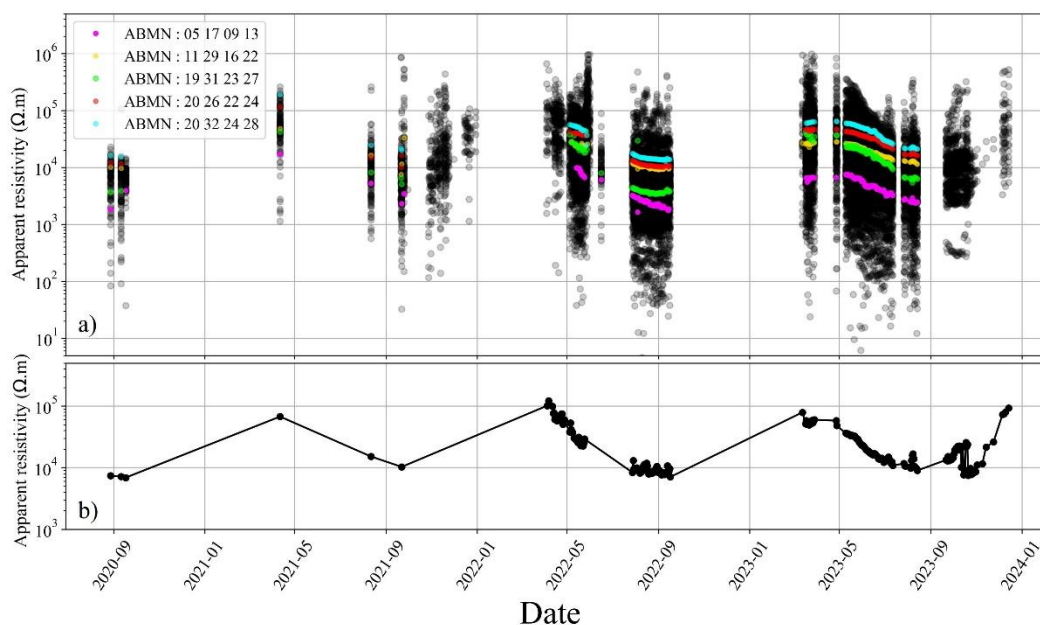
## 326 **5. Results and interpretation**

327           Selected datasets are presented below to address the objectives of this study, including  
328 the characterization of the general structure, seasonal variations, and the hydrogeological  
329 system.

### 330 **5.1. Overview of the raw data**

331           Our interpretation of the ERT data starts with an analysis of the measured apparent  
332 resistivity data, which can provide insights into subsurface conditions. Figure 3 shows the  
333 temporal distribution of the measured apparent resistivities and the averaged apparent resistivity

334 along the S-profile, with examples of time series of measured apparent resistivities obtained  
 335 using various quadrupole configurations (ABMN), shown in different colors. The majority of  
 336 measured apparent resistivities are distributed over three orders of magnitude (100  $\Omega$ .m to 100  
 337 k $\Omega$ .m), with few data points out of this range.

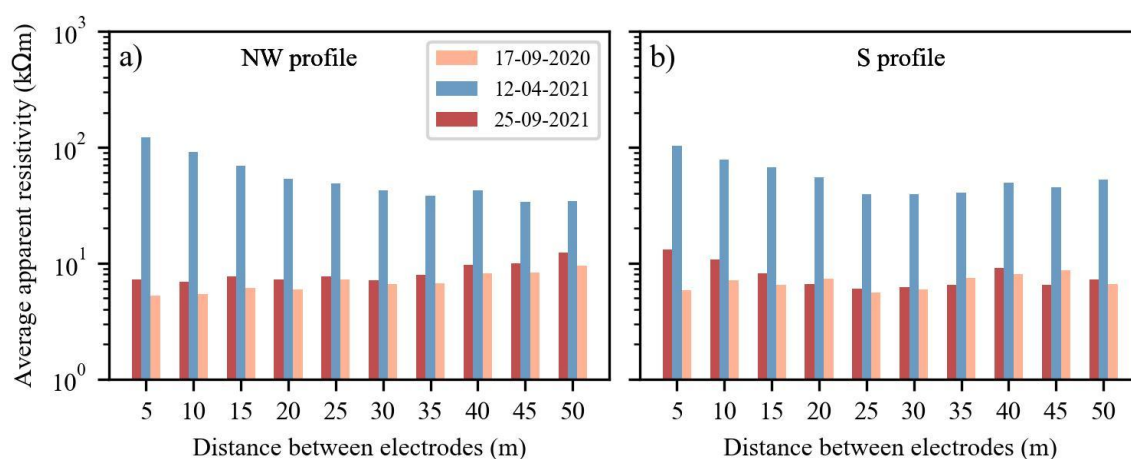


338  
 339 **Figure 3.** Distribution of measured apparent resistivity. a) daily distribution of the apparent  
 340 resistivity over time at the S face (approximately 300 datasets). Colored lines present examples of  
 341 resistivity times series, each corresponding to a different set of quadrupoles (AMNB). b) Mean daily  
 342 measured apparent resistivity at the S face.

343  
 344 Figure 4 shows the variations in the average apparent resistivity associated with the  
 345 same electrode distance or pseudo-depth for three selected datasets from two profiles (NW and  
 346 S profiles). The data reveal the interannual and seasonal variations in the measured apparent  
 347 resistivity, as well as the differences between the two sides. During frozen conditions at the  
 348 surface (dataset from 12-04-2021), the apparent resistivity is almost the same on both sides  
 349 (~100 to 120 k $\Omega$ m near the surface), with only a slight decrease with depth at both sides. At the  
 350 end of summer (dataset from 17-09-2021 and 25-09-2021), the resistivity values are higher in  
 351 2021 than in 2020 on both sides, which correlates with climatic data indicating that 2021 was a

352 cooler year, on average (see Fig. 2). Secondly, on the NW face, the average resistivities increase  
 353 with depth (from  $\sim 7$  k $\Omega$ .m to  $\sim 12$  k $\Omega$ .m), while on the south side, the average resistivities  
 354 decrease with depth (approximately 13 k $\Omega$ .m at shallow depth to  $\sim 7$  k $\Omega$ .m at greater depth).  
 355 This difference in trend between the two sides can be attributed to cooler conditions on the  
 356 north-face, where permafrost appears at shallow depth, and warmer conditions on the south-  
 357 face, characterized by a drained and thicker thawed active layer. This observation is consistent  
 358 with the temperature measurements from boreholes BH-NW and BH-S (see Fig. A1).

359



360

361 **Figure 4.** Seasonal variations of the average apparent resistivity at different distances between  
 362 electrodes within a quadrupole (*i.e.*, at varying depths of investigation). Data in spring shows the same  
 363 pattern on both sides. In autumn, there is a divergence in the trend of average resistivities with depth on  
 364 both sides, that is related to the hydrothermal conditions at each side.

365

## 366 5.2. Internal structure of the site

367 In order to gain an overview of the internal structure of the study site based on the  
 368 resistivity distribution, we carried out inversions of the first dataset acquired along two long  
 369 profiles (NW+S and NW+E), using Wenner electrode arrays with 64 electrodes (Figs. 5 and 6).  
 370 Figure 5 shows the electrical resistivity tomogram from late summer 2020 (August 26th, 2020),  
 371 where acquisition on both North-West and South sides (NW+S) was performed. The tomogram  
 372 clearly reveals the site's internal structure, with low resistivity areas (warm-colored zones)

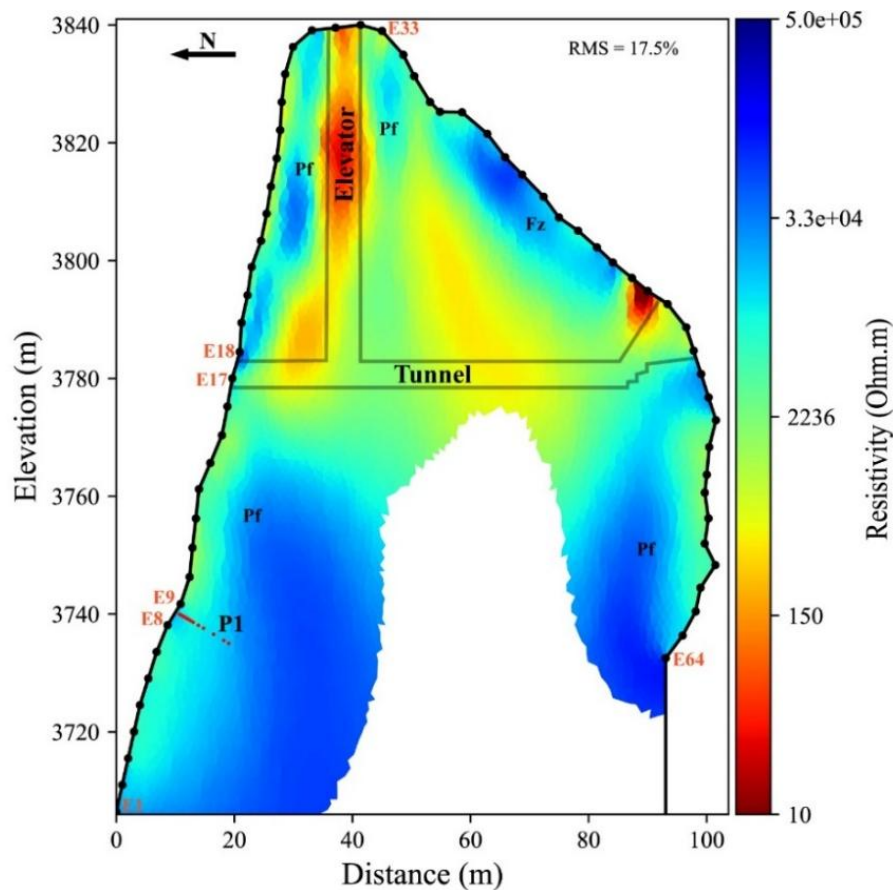
373 indicating the relative positions of the infrastructure elements (elevator and galleries on both  
374 sides). It also shows the extent of the active layer (moderate resistivity areas near the surface),  
375 as well as the permafrost evidenced by high resistivity areas (represented in cool colors).  
376 Although the lower part of the tomogram appears similar on both the NW and S profiles, which  
377 is expected since they lie in rockwalls that are alike regarding slope and aspect (where the  
378 lowest part of the S profile is deployed on the NW face as well, see Fig 1c), significant  
379 differences are evident in the upper part (*i.e.*, above the gallery level). these differences  
380 highlight the contrast between the sun-exposed S face, composed of fractured granite (clearly  
381 visible in the field; see Fig. 1d) and exposed to strong insolation, leading to drier surface  
382 conditions and consequently higher electrical resistivity. In contrast, the shaded NW face  
383 mainly consisting of massive granite and less influenced by atmospheric heat flux, remains  
384 wetter and thus leads to lower resistivity close to surface. The upper part of the profile therefore  
385 reveals strong thermal gradient typical of high-alpine summits (Noetzli et al., 2007; Magnin et  
386 al., 2017). The high-resistivity area thus appears limited, likely due to the heat flux from the  
387 sun-exposed and warm face towards the close shaded-face.

388

389

390

391



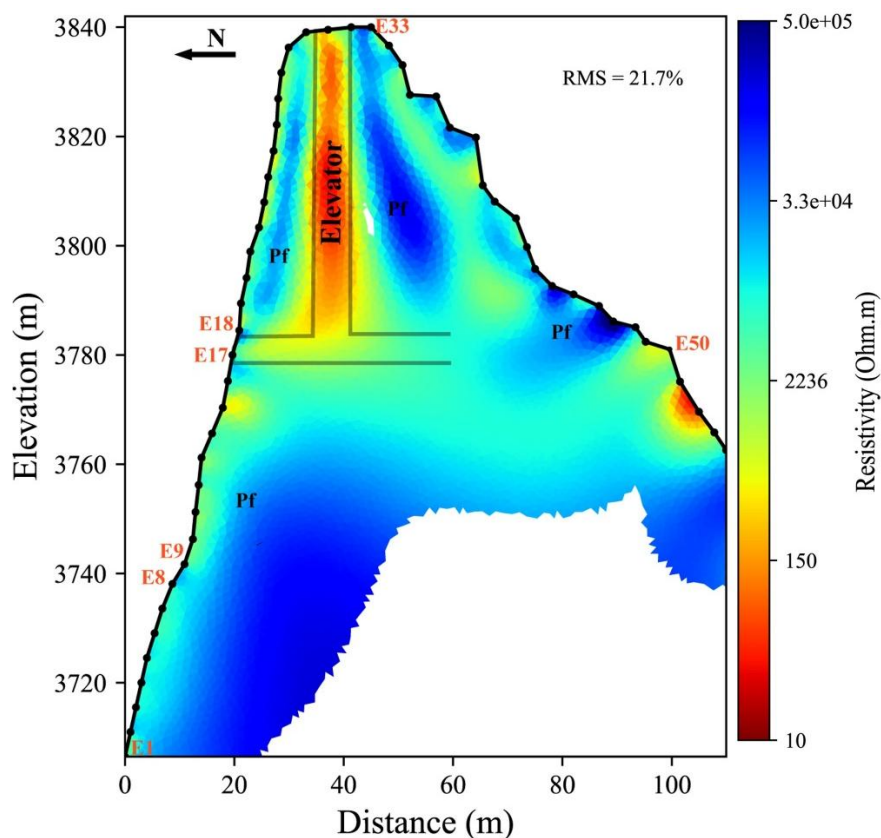
392

393 **Figure 5.** Electrical resistivity tomogram over the NW+S profile measured on August 26, 2020. A total  
 394 of 320 data points used for the inversion (475 data points constitute the complete pseudo-section), about  
 395 30% of dataset was filtered). Grey lines indicate the approximative positions of infrastructure (galleries  
 396 and elevator). Pf stands for Permafrost zone and Fz for Fractured zone. E1 to E64 are Electrode numbers.  
 397 Red dots at P1 indicate positions of the thermal sensors in BH-NW.

398

399 Figure 6 provides an example of the resistivity tomogram for the combined NW and E profiles.

400 This tomogram highlights the changes in resistivity associated with permafrost, active layer,  
 401 and anthropogenic installation (such as the elevator and gallery (relatively far from the profile  
 402 at the E side compared to S profile)). On the eastern side, a thick and desiccated active layer (>  
 403 5 m depth) is observed, with some resistive zones near the surface. Indeed, these resistive zones  
 404 are likely fractured zones creating an unsaturated and air-filled zone and surrounded by  
 405 moderate resistivity regions where fractures are filled or where water drainage is weak or  
 406 absent.



407

408 **Figure 6.** Electrical resistivity tomogram over the profile NW+E at the end of summer (September 25  
 409 th, 2021). A total of 310 data points were used for the inversion (475 data points constitute the complete  
 410 pseudo-section), about 35% of dataset was filtered). The last 10 electrodes from the E profile were  
 411 removed during processing due to connection issues. Pf stands for Permafrost zone

412

### 413 5.3. Seasonal and interannual variations

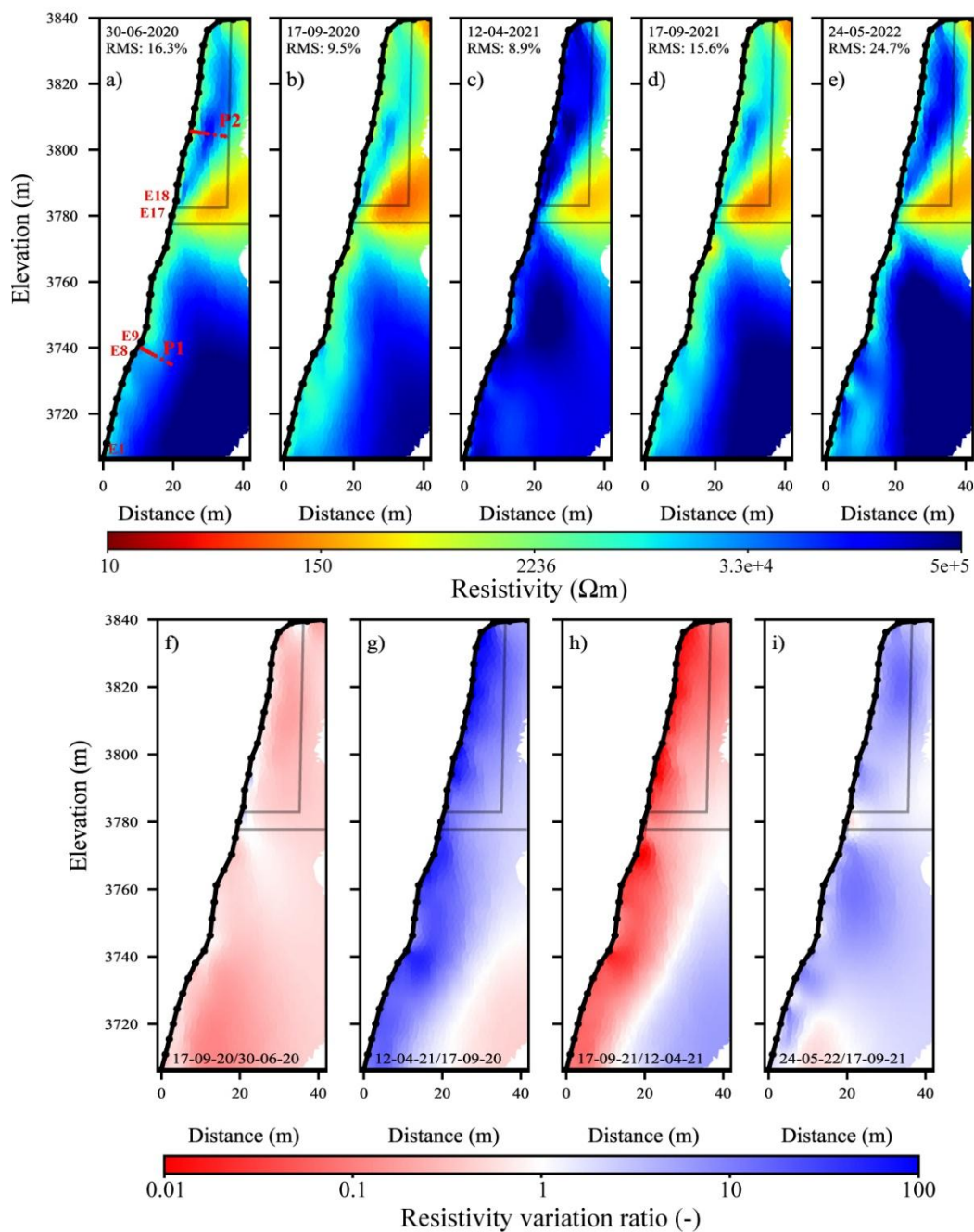
414 In order to track the seasonal and interannual variations in the permafrost, a time-lapse  
 415 inversion approach was employed to invert datasets for each profile (NW, S), while the data at  
 416 the east profile was excluded from this analysis due to significant data gaps caused by poor  
 417 electrical connection and cable malfunctions. Figure 7 shows the tomograms of resistivity  
 418 distribution after a time-lapse inversion of selected datasets acquired along the NW profile at  
 419 different time intervals. A more complete times series is presented in appendix D, while the  
 420 results from the south profile are discussed in section 5.6). Spatial and temporal changes in  
 421 resistivity can be observed, while the anomaly related to the gallery (the warm-colored area

422 (low resistivity area) remains relatively consistent over time. The permafrost layer associated  
423 with high resistivity, is observed in two zones, above and below the gallery. 2021 was, on  
424 average, cooler than both 2020 and 2022 in coherence with air temperature (Fig. 2), and this is  
425 reflected in the tomograms by a more prominent cool-colored zone (indicating colder  
426 conditions) in 2021 compared to data in 2020 (Fig. 7b and d). Additionally, there is a significant  
427 variation in the lower part of the tomograms in 2022 (Fig. 7e), which may be related to water  
428 infiltration in fractures that shortcut the heat transfer from the surface to depth (Hasler et al.,  
429 2011). However, this area is uncertain, as it is located at the border of the tomogram where  
430 sensitivity is low. In addition, the RMS error is high in this tomogram, indicating high  
431 uncertainties. Therefore, this information should be carefully considered and verified with  
432 further measurements focused on the zone of interest. Unlike Offer et al. (2025), no evidence  
433 of water pressurization was observed from the geophysical measurements on the NW face. This  
434 is most likely due to the distance between the monitored area and the water table laying at about  
435 1000 m lower (Magnin and Josnin, 2021), and that leads to water drainage.

436         Instead of analyzing temporal resistivity changes in absolute terms, Figure 7 (f - i)  
437 illustrates the resistivity variation ratio between two subsequent measurements. This approach  
438 facilitates the tracking and visualization of small changes in resistivity. A value of 1  
439 (represented in white color) corresponds to no change in resistivity between the two  
440 measurements (reflecting consistent thermal/hydrological conditions over time), while the blue  
441 color indicates that the resistivity increased over time, and the red color represents the inverse.  
442 It can be observed that seasonal variations are the most pronounced, as illustrated in Figure 7g,  
443 h and i, compared to short-term fluctuations (see Fig. D2). The effects of freezing and thawing  
444 are marked by maximum variations near the surface (in the active layer). In contrast, over a  
445 short time interval (*i.e.*, a few weeks), only minor variations are noted (*e.g.*, Fig. 7f, Fig. D2 b,  
446 e and j). The decrease in resistivity near the surface at approximately 3780 m, observed in

447 Figure 7i, could be related to water flow around the gallery, where water circulation and  
448 percolation in the galleries occurs every summer (Ben-Asher et al., 2025). Consequently, a  
449 specific water diversion system has been installed to protect tourists from these water flows.  
450 Furthermore, at approximately 3740 m, close to borehole BH-NW, we observe variations in  
451 resistivity, with values higher than in the surrounding zone, forming a vertical pattern visible in  
452 Figures 7b, d, and e. These features coincide with open sub-vertical fractures that affect the  
453 temperature-depth profile in boreholes (Magnin et al., 2015).

454



455

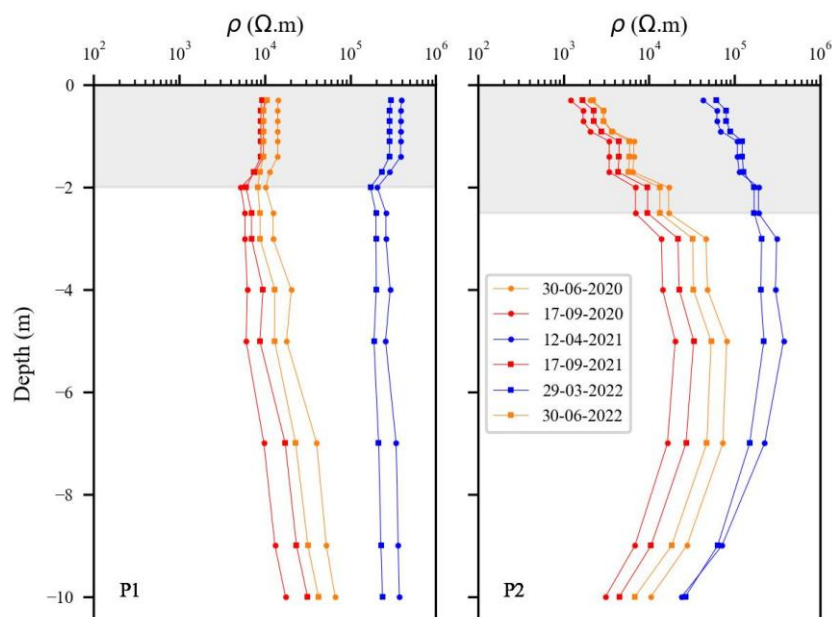
456 **Figure 7.** Seasonal and interannual variations of electrical resistivity at NW side. a - e) electrical  
 457 resistivity tomograms at different dates (from June-2020 to June-2022). The conductive zone (in warm  
 458 colors) denotes the presence of the gallery and elevator (see Fig. 5). The red dots (P1 in panel a) indicate  
 459 the positions of the thermal sensors in the borehole BH-NW. Data presented on Figures 8, 10 and 11 are  
 460 extracted at the red dots (P1 and P2). f - i) resistivity variation ratio between consecutive electrical  
 461 resistivity tomograms. Blue colors indicate an increase in resistivity, while red colors represent a  
 462 decrease in resistivity from one measurement to the next.

463

464

#### 465 **5.4. Virtual borehole analysis**

466 Inverted resistivities were extracted along profiles P1 and P2, corresponding to borehole  
467 BH-NW and a virtual borehole, respectively (see positions of P1 and P2 in Fig. 7a). The  
468 extracted resistivities (Fig. 8) show that the variation of resistivity with depth is more  
469 pronounced at P2 than at P1. This greater variation could be due to a higher water content in  
470 the active layer or a thicker active layer at P2 compared to P1. The greater thickness of the  
471 active layer in the upper section can be explained by the 3D heat transfer and the proximity of  
472 the shaded face (NW side) to the sun-exposed faces (S side) in the top part (Magnin et al.,  
473 2017), as well as the greater amount of direct sun-beams at the summit than in the more shaded  
474 lower parts of the face. The 3D effects are well visible at depth of P2, where resistivity decreases  
475 due to warmer conditions close to the opposite sun-exposed face. In the lower section at P1, the  
476 contrast between the resistivity in the active layer and that in the permafrost is not significant.  
477 This may be attributed to (i) reduced thermal variability because of snow accumulation in this  
478 zone (see Fig. 1c), where the snowpack acts as a thermal insulator, reducing temperature  
479 variability; (ii) the presence of fractures (as noted above) influencing the temperature-depth  
480 profile (see Fig. 7b, e and d). However, it is important to note that the ALT is about 2.7 m at  
481 the end of summer (based on BH-NW measurements; see Fig. A1), whereas, the smallest  
482 quadrupole spacing is 15 m, leading to effective depth around 2.55 m (Edwards, 1977), which  
483 is insufficient to fully capture the resistivity variations near the surface. Additionally, a slight  
484 decrease in permafrost resistivity is observed between 30 June 2020 and 30 June 2022. That is  
485 consistent with the observed permafrost warming at 10 m depth (Magnin et al., 2024). Finally,  
486 in 2021, resistivity values were higher in both the upper and lower parts (at P1 and P2)  
487 compared with 2020 and 2022, consistent with the temperature measurements (see Fig. 2, or  
488 details in Magnin et al. (2024)).



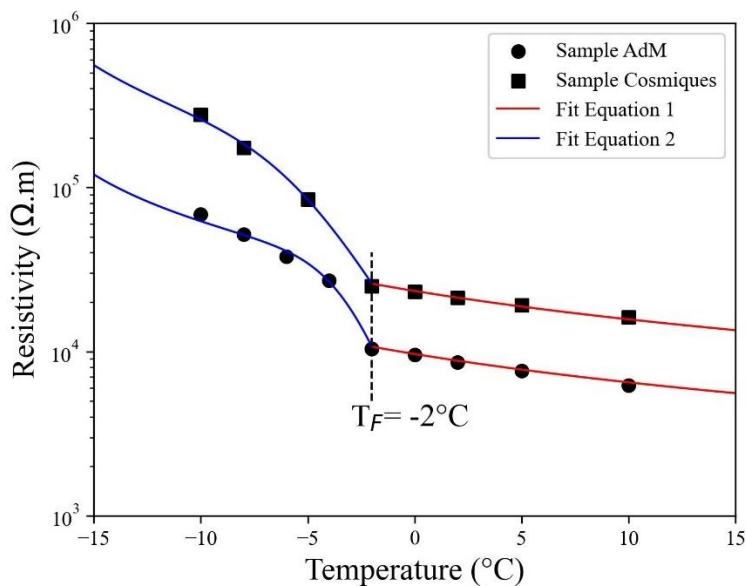
489  
 490 **Figure 8.** Resistivity extracted over depths at different dates and locations (P1, P2). Resistivities are  
 491 extracted from tomograms in Fig. D1. There is greater variation at the higher profile (P2), where heat  
 492 transfer from the nearby sun-exposed faces is more significant in the site's upper part.

493

### 494 5.5. Temperature - resistivity relationship

495 Figure 9 presents the measurement results for the granite sample from the study site  
 496 (labeled Sample AdM), alongside measurements of another granite sample (Sample  
 497 Cosmiques) collected from a nearby site at the lower Cosmiques Ridge (Mont-Blanc massif,  
 498 3613 m a.s.l.), as reported by Duvillard et al. (2021). The experimental datasets are presented  
 499 along with data fits, using Equations 1 for temperatures above the freezing point, and Equation  
 500 2 for temperatures below the freezing point. The model proposed in Section 3 successfully fits  
 501 the data above and below the freezing temperature, providing a proxy for connecting electrical  
 502 conductivity or electrical resistivity measured in field to temperature.

503



504

505 **Figure 9.** Resistivity-temperature relationship from laboratory measurements on two granite samples  
 506 from (1) the study site (Sample AdM), and (2) from the Cosmiques ridge, Mont-Blanc massif, West  
 507 (3613 m a.s.l.) (Sample labeled Cosmiques).  $T_F$  denotes the freezing temperature. The solid lines  
 508 correspond to the fits using the Equation 1 (red lines) and Equation 2 (blue lines), in unfrozen and frozen  
 509 conditions, respectively. The parameters of the model in Equation 2 are ( $T_C = -1.3$  °C,  $\theta_r = 0.004$ ,  $\sigma(T_0) =$   
 510  $2.3 \times 10^{-4}$  S m<sup>-1</sup>) for Sample AdM, and ( $T_C = -2.17$  °C,  $\theta_r = 0.004$ ,  $\sigma(T_0) = 9.5 \times 10^{-5}$  S m<sup>-1</sup>) for Sample  
 511 Cosmiques.

512

513 Extracted resistivities at P1 are superimposed on the co-located borehole BH-NW,  
 514 where temperature measurements are available. We are using these two datasets (*i.e.*,  
 515 temperature and resistivity measurements at the same location, BH-NW) to explore the  
 516 potential for estimating temperature based on electrical resistivity measurements and to perform  
 517 a quantitative evaluation of the temperature - resistivity relationship determined in a laboratory.

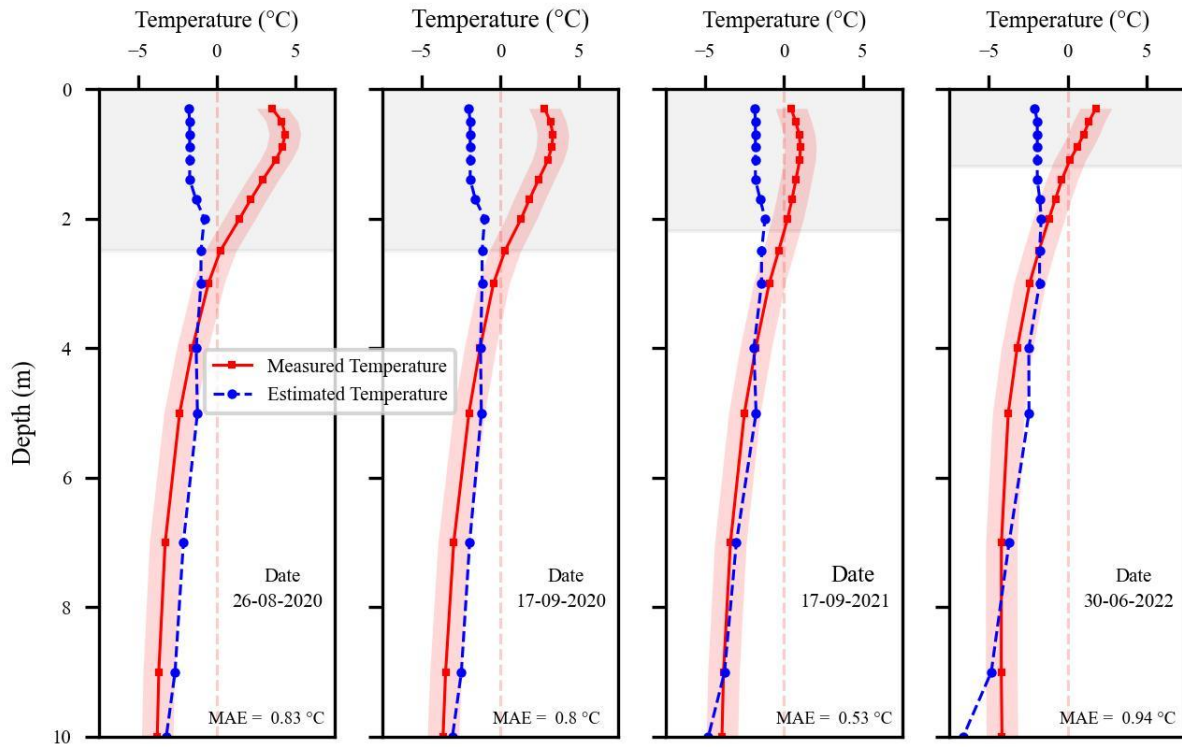
518 It is well established that when temperature  $> 0$  °C (*i.e.*, the case in the active layer),  
 519 electrical resistivity depends on multiple factors, including porosity, water content, water  
 520 salinity, Cation Exchange Capacity (CEC) and temperature (Revil et al., 2018). This multiple  
 521 parameter dependence makes it difficult to accurately model or predict electrical resistivity, or  
 522 to use it as a proxy for temperature estimation in the active layer. In contrast, under frozen  
 523 conditions, resistivity of the medium is primarily controlled by the remaining unfrozen pore

524 water, which is largely temperature dependent, while other parameters can be assumed  
525 relatively constant.

526         Based on this assumption, the resistivity values extracted from inverted model of  
527 resistivity were converted to temperature using the petrophysical model in Equation 2  
528 (Duvillard et al., 2021; 2018; Coperey et al., 2019). Figure 10 shows the measured temperature  
529 alongside the estimated temperature from ERT data, plotted against depth at different dates (in  
530 summer and autumn). A good agreement is observed between the measured and estimated  
531 temperature in frozen zone, with mean absolute error (MAE) less than 1 °C within the frozen  
532 zone (approximately from 2-2.5 m to 10 m, depending on the date). These results suggest that  
533 the temperature distribution across the site can be reasonably estimated using this model,  
534 assuming that the medium is sufficiently homogeneous and that resistivity variations are  
535 predominantly controlled by temperature. Figure 11 illustrates the temperature distribution  
536 along the profile NW estimated from electrical resistivity measurements acquired at different  
537 dates between June 2020 and June 2022. The estimated temperatures consistent with previous  
538 analyses and highlight two permafrost zones located above and below the gallery. A clear  
539 temperature gradient with depth is observed on the 2D temperature sections, with positive  
540 temperatures around and in the infrastructure. It can also be observed that temperature decreases  
541 with depth, reaching values lower than -5 °C in the zone where ERT sensitivity is low or absent  
542 (see lower part of profile NW Fig 11). At greater depths, the reduced sensitivity affects the  
543 reliability of temperature estimates.

544         Finally, data collected under frozen surface conditions (*i.e.*, measured in winter and  
545 early spring, when contact resistance is high) shows large discrepancy between the estimated  
546 and measured temperature and therefore cannot be reliably used for temperature estimation.

547

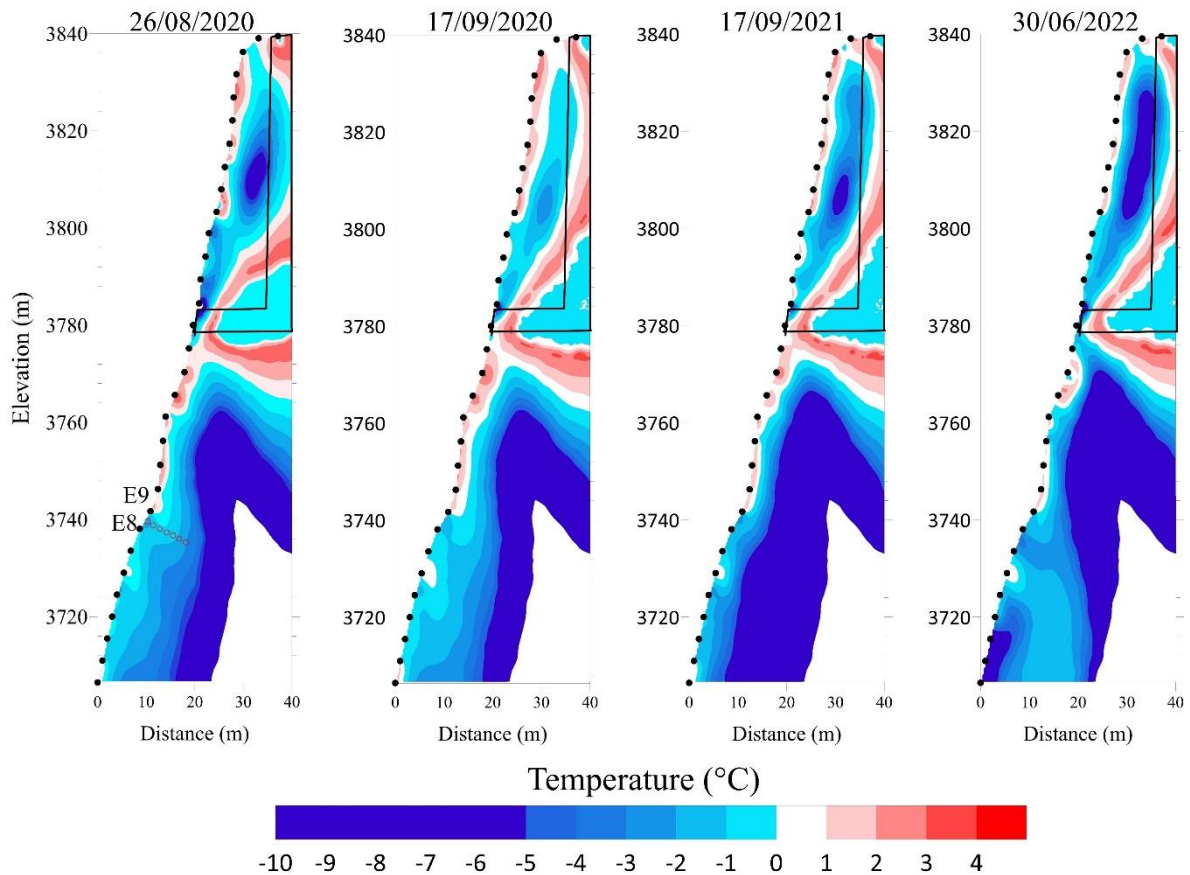


548

549 **Figure 10.** Comparison between measured temperatures in BH-NW and estimated temperatures derived  
 550 from geophysical measurements (*i.e.*, extracted resistivity values at different dates) using the  
 551 petrophysical model in Equation 2. The gray-shaded area indicates the extent of the active layer at the  
 552 time of measurement. The red-shaded zones show the  $\pm 1$  °C range around the measured temperature.  
 553 The mean absolute error (MAE, in °C) quantifies the average error within the frozen zone for each date.

554

555

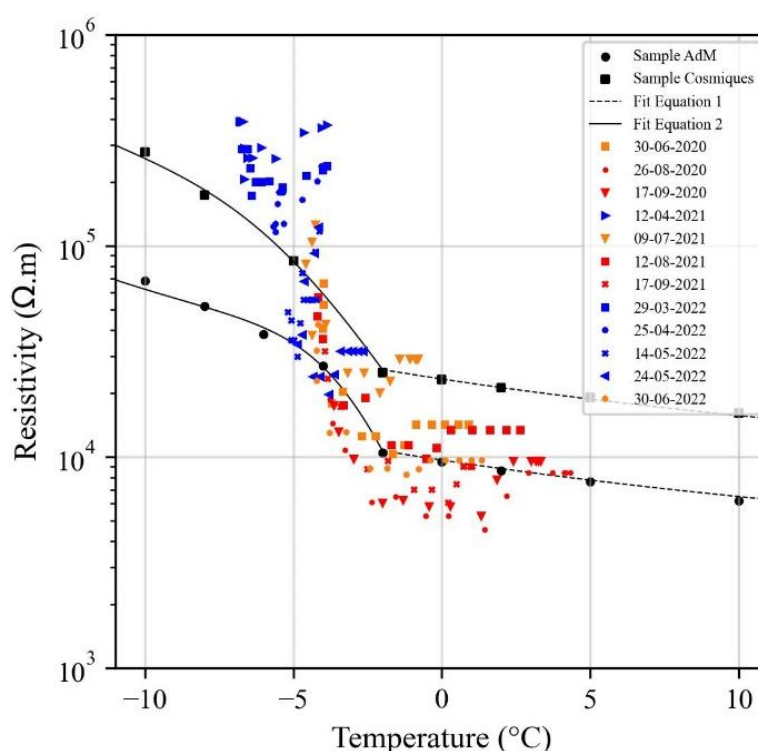


556  
 557 **Figure 11.** Spatio-temporal evolution of subsurface temperatures along the NW profile derived from  
 558 electrical resistivity measurements, using Equation (2) and parameters obtained from laboratory  
 559 measurements. Black dots indicate the electrode positions. The red circles indicate the location of  
 560 borehole BH-NW, while the black lines mark the relative positions of the gallery and the elevator. The  
 561 blanked zones in the lower part of the profile correspond to areas of low sensitivity of the geophysical  
 562 measurements and are therefore not reliable to temperature estimation.

563

564 To go further in our analysis, Figure 12 shows the extracted resistivity at P1 vs.  
 565 temperature data measured in co-located BH-NW at different dates. Laboratory measurements  
 566 on two granite samples (labeled Sample AdM and Sample Cosmiques) are also shown. Three  
 567 key observations can be made: i) Data collected in winter and spring (frozen conditions at  
 568 surface), presented by blue symbols, show resistivity values higher than those expected from  
 569 laboratory measurements, which aligns with the field observations reported by Maierhofer et al  
 570 (2024). This may be related to the salt segregation during freezing, which may enhance

571 conductivity of pore water and consequently reduce resistivity of samples. ii) At higher  
 572 temperature (unfrozen conditions at surface), a linear trend is observed that aligns with  
 573 laboratory measurements for part of datasets (e.g., datasets of 26/08/2020 and 17/09/2020). The  
 574 difference in resistivity between field and laboratory data under unfrozen conditions could be  
 575 attributed to the heterogeneity at the field scale and/or the difference in water content and water  
 576 salinity between laboratory and field environments. Whereas laboratory measurements were  
 577 conducted in saturated conditions (saturation was performed under vacuum using degassed  
 578 water). iii) Field data exhibit greater dispersion compared to laboratory data, which can be  
 579 attributed to several factors, including 3D effects at the site, the influence of infrastructure and  
 580 heterogeneity at different scales (from fractures scale to pore scale). In addition, there is a  
 581 difference in resolution between the two field measurements: temperature measurements are  
 582 local, while resistivity measurements account for a larger volume.



583  
 584 **Figure 12.** Resistivity vs. temperature. Resistivities are extracted from the tomograms in Figure D1 at  
 585 location P1. Temperature is measured by sensors at BH-NW. Laboratory data on two granite samples  
 586 and fitting with Equation 1 and 2 are shown too.

## 587 5.6. Hydrogeological dynamics

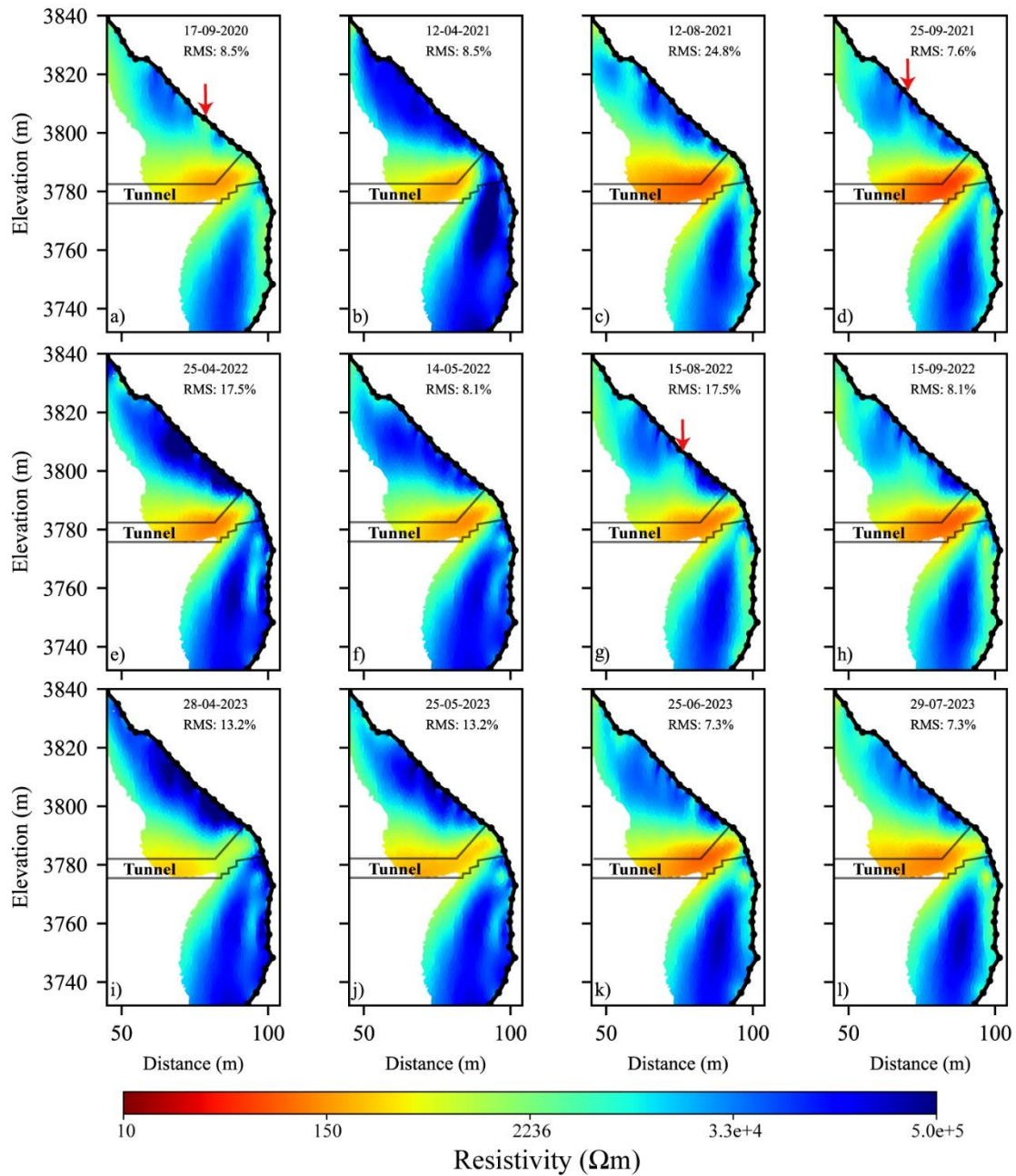
588 One of the objectives of this study was to assess hydrogeological dynamics. Due to gaps  
589 in the ERT time series, the analysis of times series did not yield conclusive information.  
590 Therefore, we selected specific datasets (nearly complete pseudo-sections) and compared the  
591 results of the time-lapse inversion to gather information about water infiltration and drainage.  
592 Although we could not precisely identify the infiltration and drainage pathways or the water  
593 table (which may be located at a lower altitude according to Magnin and Josnin (2021)) using  
594 ERT measurements, we observed several instances that serve as evidence of possible water  
595 flows.

596 Figure 13 shows the results of the time-lapse inversion of datasets along the S profile at  
597 various time intervals. The same inversion parameters were applied as those used to invert the  
598 datasets on the NW side (Fig. 7). In the upper part of the profile (*i.e.*, above the gallery), we  
599 interpret that seasonal variations in resistivity are influenced by the presence of fractures, which  
600 control water flow pathways and, consequently the resistivity response throughout the seasonal  
601 cycle. This portion of the profile is exposed to strong insolation in summer, which dries the  
602 rock and fractures, leading to an increase in resistivity near the surface due to air-filled pores  
603 and fractures (*e.g.*, Fig 13b, c and l). Conversely, decreases in resistivity in this zone (*e.g.*, Fig  
604 13a, d and g), can be attributed to higher water saturation caused by the circulation of snowmelt  
605 or rainfall water. Snowmelt on this side supplies substantial amounts of water throughout the  
606 thawing season (Ben-Asher et al., 2023). The conductive zone observed beneath the desiccated  
607 area (*e.g.*, Fig. 13d and h) likely corresponds to zone of increased water saturation, as also  
608 reported by Sass (2004).

609 In the lower part of the S profile (*i.e.*, below the gallery), the seasonal variations in  
610 permafrost resistivity are clearly observed and can be tracked over time, with no evidence of  
611 significant water flow or drainage in this zone. This portion of the S profile shares a similar sun

612 exposure to the NW profile and therefore exhibits comparable dynamics, with the development  
 613 of a thawed and more water saturated active layer than in the upper part, because it is less  
 614 exposed to solar radiation, it undergoes less desiccation than the south face sector.

615



616

617 **Figure 13.** Tomograms of resistivity along the south side (S profile). Electrical resistivity tomograms at  
 618 different dates (from September-2020 to July-2023). The conductive zone (in warm-colors) explained  
 619 by the presence of the gallery. The red arrows indicate the potential zones of water infiltration from  
 620 snowmelt or precipitation.

621

## 622 6. Discussion

623 In this study, we use repeated and automated ERT to investigate the evolution of  
624 permafrost at a high altitude rockwall site. As expected, data from A-ERT are of lower quality  
625 compared to manual measurements, where the operator can intervene to improve CR after each  
626 electrode check (Doetsch et al., 2015; Hilbich et al., 2009). High CR is the main challenge  
627 preventing the year-round collection of high quality data at high altitude rockwall sites such as  
628 the site investigated in this study. Therefore, conducting ERT in frozen surface conditions on  
629 rockwall permafrost remains challenging because of the high CR. Various approaches were  
630 tested to improve CR. For instance, duplicated electrodes provided a durable and significant  
631 improvement in CR (~ one order of magnitude reduction), helping to enhance data quality.

632 Time lapse inversion of the measured resistivity showed the seasonal and interannual  
633 variations (Fig. 7, 8 and 13). We observe that resistivity decreased over time at greater depths  
634 (*e.g.*, at P1 and P2, comparing data from July 30, 2020, and July 30, 2022), indicating  
635 degradation of the permafrost as also revealed by borehole measurements (Magnin et al., 2024).  
636 However, this decrease in resistivity is minor, likely due to the relatively short observation  
637 period of two years at NW side and four years at S side. A thicker active layer is observed at  
638 the upper section, which can be attributed to 3D heat transfer processes and the close proximity  
639 of the shaded north-west face to the sun-exposed southern faces in the upper part of the slope  
640 (Magnin et al., 2017; Noetzli et al., 2007).

641 The contrast between the resistivity in the active layer and that in permafrost is not  
642 significant in the lower section on the NW side at BH-NW (P1 Fig. 8), which may result from  
643 low ice content/water content where the porosity is around 1 %, the insulating effect of snow  
644 accumulated in the zone of the BH-NW or due to high surface conductivity in granite. The  
645 alteration of granite involves the transformation of primary minerals (mica and alkali feldspars)  
646 into secondary clay minerals (such as kaolinite), which are known for their high cation

647 exchange capacity and, consequently, their contribution to surface conductivity (Piolat et al.,  
648 2025; Revil et al., 2024). Additionally, the sensitivity of the used electrode array (with a  
649 smallest quadrupole length of 15 m) could affect the resolution of ERT image near the surface  
650 (Binley and Kemna, 2005).

651         One of the objectives of this study was to evaluate the potential of using field resistivity  
652 measurements to provide 2D or 3D information on thermal distribution in permafrost, based on  
653 the superposition of resistivity and temperature datasets. The temperature estimation based on  
654 ERT data leads to good agreement with observed temperatures, with a mean absolute error less  
655 than 1 °C at depths between 2.5 to 10m, indicating that the proposed model (Equation 2) can  
656 reasonably reproduce subsurface permafrost temperatures. Consequently, this approach can  
657 provide valuable insights into the site's thermal distribution as shown in Figure 11, even though  
658 internal permafrost temperatures typically lie just a few degrees below freezing (e.g., Noetzli  
659 et al., 2024). However, a precision of  $\pm 1$  °C may be insufficient in permafrost studies, where  
660 minor temperature variations can greatly impact stability and long-term thermal evolution.  
661 Nevertheless, this level of accuracy remains within the uncertainty range commonly reported  
662 for thermal models (Magnin et al., 2017).

663         On the other hand, predicting temperature in the active layer remains challenging, as  
664 temperature is not the dominant factor affecting resistivity in thawed conditions. Data collected  
665 under frozen surface conditions (*i.e.*, measurements taken in winter and spring with high contact  
666 resistance) resulted in larger discrepancy between estimated and measured temperature and  
667 could not be reliably used for temperature estimation. Consequently A-ERT measurements  
668 remain challenging when the ground surface is frozen, mainly due to the high contact resistance.

669         Furthermore, the transition between frozen and unfrozen conditions is not clearly  
670 distinguished at resistivity curve extracted from field measurements (see Fig. 8, 10). The  
671 freezing point, which is expected to result in a significant change in resistivity (as observed in

672 laboratory measurements), does not exhibit the same effect in field. However, some datasets  
673 (e.g., datasets of 12/08/2021 and 17/09/2021) show progressive increase in resistivity when  
674 temperature decreased (*i.e.*, indicating progressive freezing). This point needs to be addressed  
675 in further research with a smaller electrode array to improve the resolution of geophysical  
676 measurements.

677 On the sun exposed face, the tomograms of resistivity show near-surface pore  
678 desaturation, attributed to strong insolation on the rock face that is perpendicular to the sun  
679 beam, along with features that may relate to water infiltration along fractures. The exact  
680 pathways of infiltration and drainage are still ambiguous, possibly due to the resolution of  
681 resistivity measurements. With the AdM setting, we can also hypothesize that the saturated  
682 conditions are almost never reached. There is water circulation, but no pressurization or  
683 development of a water column, because the water table is likely lower than the area covered  
684 by the measurements (Magnin and Josnin, 2021), conversely to Offer et al. (2025) at the  
685 Kitzsteinhorn for example. Indeed, our investigation is in a different setting: high altitude peak  
686 lying ~1000 m above the water table (Magnin and Josnin, 2021) while in the Kitzsteinhorn  
687 outcrops from a glaciated areas with a probably much closer water table.

688 Finally, A-ERT acquisition using smaller electrode array can improve near surface  
689 resolution and provide more detailed information about the subsurface. Combining ERT with  
690 other geophysical methods, such as induced polarization and/or refraction seismic tomography,  
691 can also provide complementary petrophysical and spatial sensitivity, enabling a more  
692 comprehensive investigation of the hydrogeological system of high mountain permafrost.

693

## 694 **7. Conclusions**

695 We used repeated and Automated Electrical Resistivity Tomography (A-ERT) to  
696 monitor permafrost dynamics over nearly four years at AdM in the French Alps, aiming to

697 better understand the complexities of permafrost behavior in response to climatic variations and  
698 to explore the potential of the method for quantitative monitoring. The key findings are  
699 summarized as follows:

- 700 1. Through detailed analyses of ERT data, we were able to characterize the active layer  
701 dynamics and identify significant seasonal and multiannual changes in permafrost  
702 evolution. Importantly, we observed that the ALT and permafrost conditions below  
703 varied significantly from one face to another in coherence with climate signals and  
704 measured temperatures in boreholes.
- 705 2. This research demonstrates that temperature can be quantitatively derived from  
706 geophysical measurements of electrical resistivity based on a petrophysical model  
707 connecting resistivity to temperature with precision of approximately  $\pm 1$  °C in  
708 frozen granite during summer and autumn monitoring.
- 709 3. Our assessments of the hydrogeological system revealed instances of possible water  
710 flow as well as bedrock desiccation under strong insolation. That said, the exact  
711 pathways of infiltration and drainage remain unclear.
- 712 4. The results underscore the utility of ERT as a promising, non-invasive approach for  
713 quantitative monitoring non-linear permafrost evolution in high mountains.

714 Although installation of A-ERT system is relatively low costs, it can require substantial  
715 maintenance in high-risk areas like unstable high mountain rockwalls where rockfalls and  
716 lightning effects can damaging equipment. This study highlights the urgent need to address  
717 challenges related to climate conditions at high-altitudes that affect device performance and  
718 contact resistances, in order to enhance the reliability and durability of continuous A-ERT data  
719 collection.

720

721

722

723 **Data availability.** Data will be made available on request to the corresponding author.

724 **Author contributions.** FA performed the data analysis, prepared the figures, and wrote the

725 majority of the text. JB contributed to data acquisition, writing, and figure preparation. FM and

726 AR contributed to the design of the ERT survey, as well as data acquisition and discussion of

727 the results. EM, MBA, LR and PAD contributed to the field installation and acquisition, JR

728 conducted and processed the laboratory data, MK contributed to data inversion and discussion,

729 TC provided air temperature data, PAD offered additional information about the site. Finally,

730 all authors actively contributed to the preparation of this version of the paper.

731

732 **Competing interests.** The authors declare that they have no conflicts of interest.

733

734 **Acknowledgments.** This research is part of the ANR WISPER project (ANR-19-CE01-0018)

735 and the Action Plan on Risks from Glacial and Periglacial Origin (PAPROG) from the French

736 Ministry of Ecological Transition, Biodiversity, Forest, Sea and Fishing. The authors

737 acknowledge the following persons who helped with the field work: Antoine Chabas, Bruno

738 Galabertier, Stéphane Jaillet and Raphaël Gallet from the EDYTEM Laboratory, Simon Alesina

739 from the University of Lausanne, Marc Cleriot for help, and Catherine Coulaud from IGE. The

740 authors are also grateful for the Compagnie du Mont-Blanc that provided access to the site and

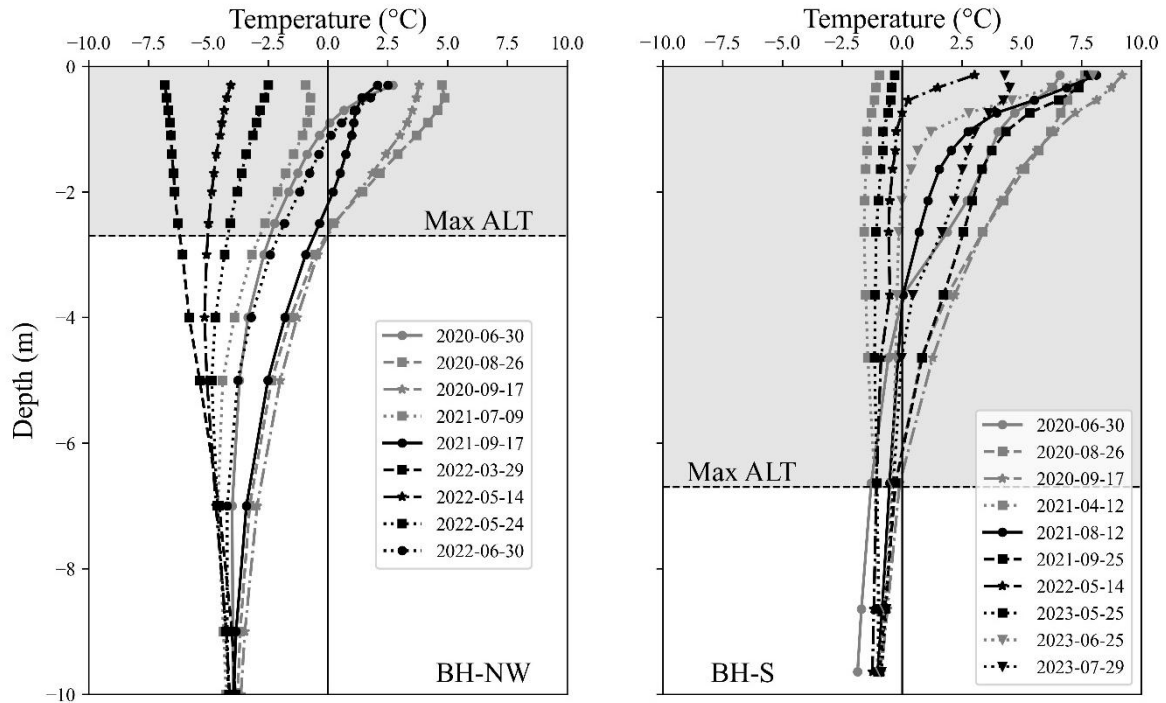
741 support. Finally, we thank Vincenzo Lapenna and the four anonymous Referees for their

742 constructive reviews, and we are especially grateful to the Editor, Teddi Herring for her

743 valuable comments during the review of this paper.

744 **Appendix A: Temperature measurements in boreholes on different date BH-NW and**

745 **BH-S**

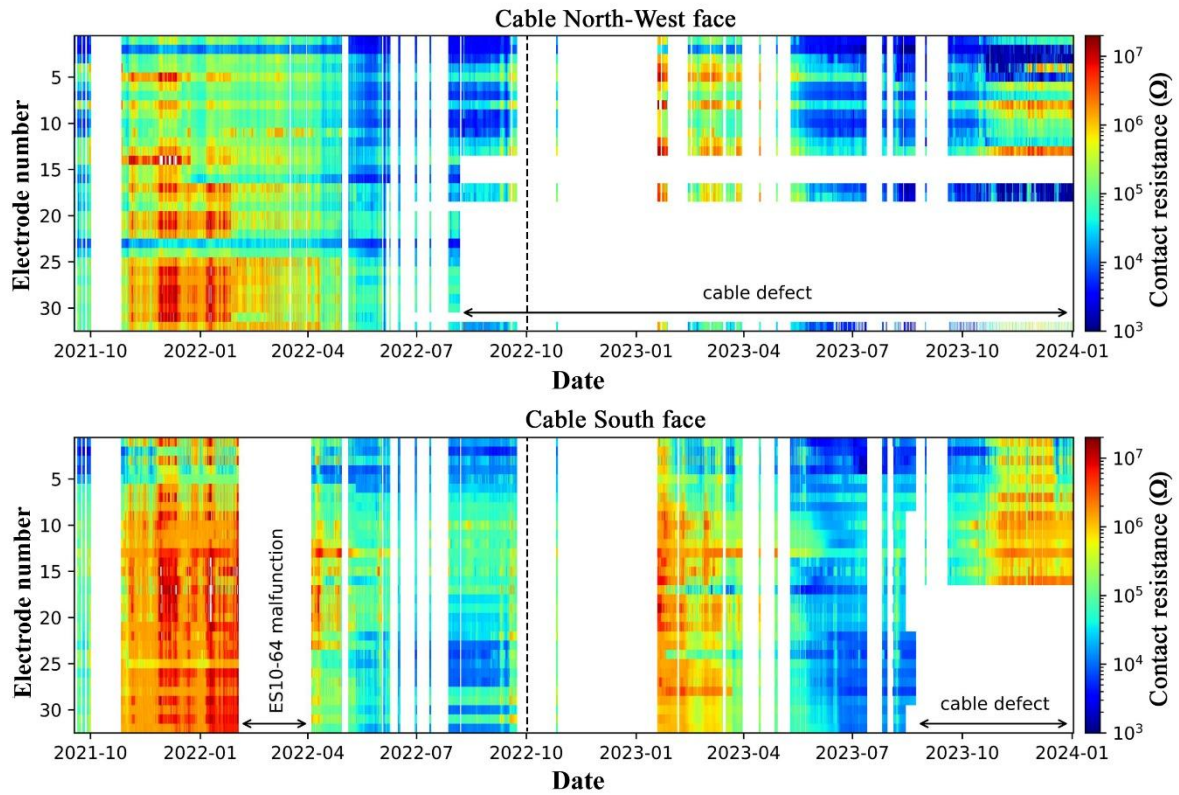


746

747 Figure A1: Temperature variation over depth in boreholes BH-NW and BH-S on different dates  
 748 aligned with the ERT measurement periods shown in Figures 7, 12 and D1. The gray-shaded area  
 749 indicates the extent of the active layer at each borehole.

750

751 **Appendix B:** Evolution of the contact resistance (CR) over time at NW and S profiles. The  
 752 CR measured before each daily measurement between 09/2021 and 12/2023 are presented in  
 753 Figure B1.



754

755 **Figure B1.** Temporal evolution of contact resistance at the North-West side and South side. Data partly  
 756 missing is due to cable defects. The vertical dashed line indicates the date at which the duplicate  
 757 electrodes were installed.

758

759

**Appendix C: Summary of data presented in this study**

760 **Table C1.** Summary of data presented in this study. Number of data before filtering is 155  
 761 datum points of Wenner configuration. Most of datasets have more than 80% of total number  
 762 of measurements. Two datasets have more than 40% of lost data because of disconnected  
 763 electrodes.

764

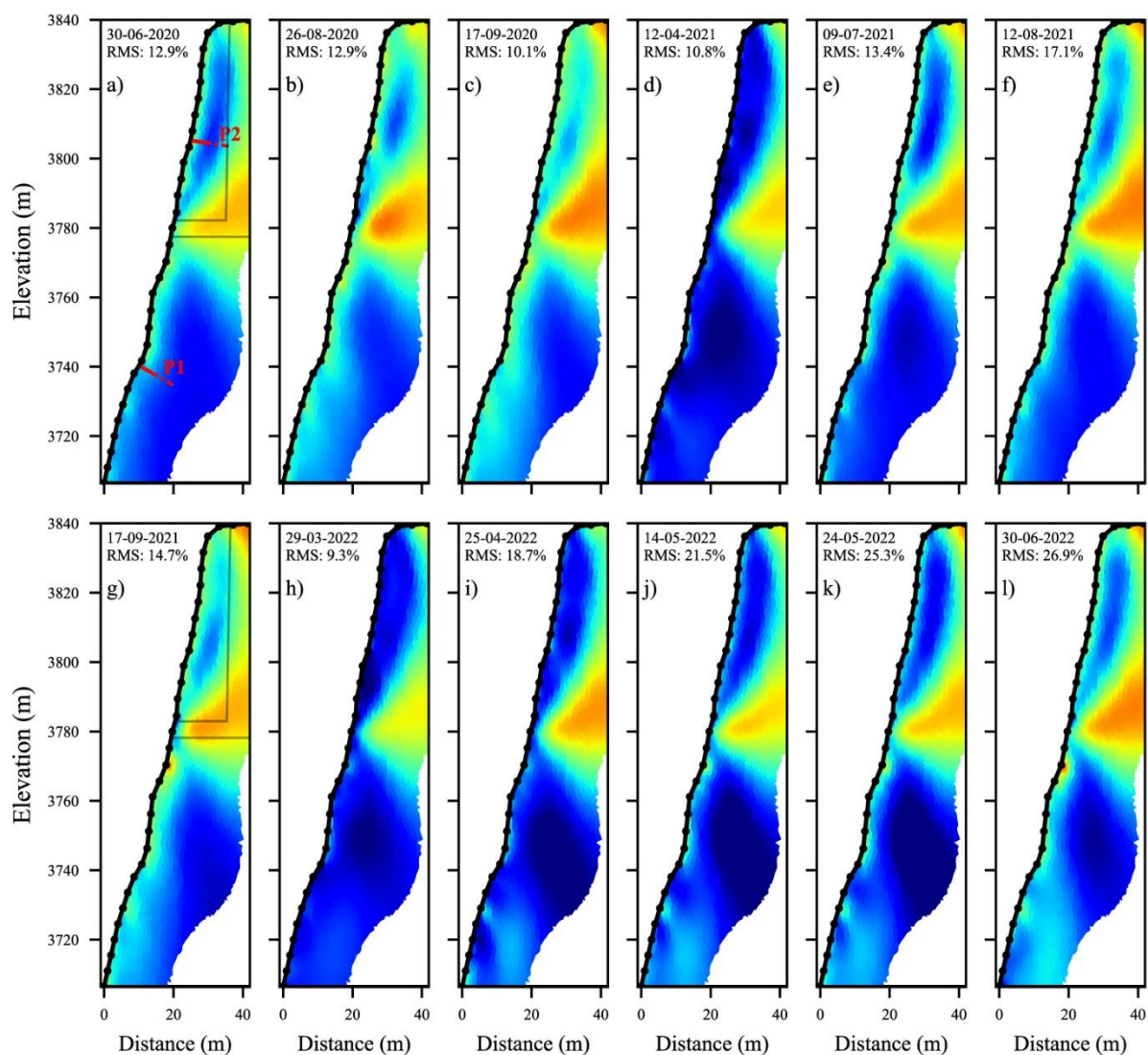
| Date       | N-W Profile                 |                | S Profile                   |                |
|------------|-----------------------------|----------------|-----------------------------|----------------|
|            | Number of data after filter | Percentage (%) | Number of data after filter | Percentage (%) |
| 30-06-2020 | 151                         | 97.5           | -                           | -              |
| 26-08-2020 | 149                         | 96.1           | 90                          | 58             |
| 17-09-2020 | 151                         | 97.5           | 90                          | 58             |
| 12-04-2021 | 118                         | 76.1           | 121                         | 78             |
| 09-07-2021 | 114                         | 73.5           | -                           | -              |
| 12-08-2021 | 149                         | 96.1           | 140                         | 90.3           |
| 17-09-2021 | 145                         | 93.5           | 131                         | 84.5           |
| 25-09-2021 | 143                         | 92.2           | 144                         | 92.9           |
| 29-03-2022 | 121                         | 78             | -                           | -              |
| 25-04-2022 | 141                         | 91             | 131                         | 84.5           |
| 14-05-2022 | 141                         | 91             | 147                         | 94.8           |
| 24-05-2022 | 140                         | 90.3           | 146                         | 94.1           |
| 30-06-2022 | 102                         | 65.8           | -                           | -              |
| 30-07-2022 | -                           | -              | 145                         | 93.5           |
| 15-08-2022 | -                           | -              | 145                         | 93.5           |
| 15-09-2022 | -                           | -              | 144                         | 93             |
| 19-03-2023 | -                           | -              | 138                         | 89             |
| 28-04-2023 | -                           | -              | 143                         | 92.2           |
| 25-05-2023 | -                           | -              | 148                         | 95.5           |
| 25-06-2023 | -                           | -              | 144                         | 92.9           |
| 29-07-2023 | -                           | -              | 140                         | 90.3           |

765

766

## Appendix D: Time-lapse inversion results

767 Appendix D presents time-lapse inversions of a large number of datasets from north-west face  
 768 and south faces. The Resistivity variation ratio between consecutive electrical resistivity  
 769 tomograms is also evaluated. A summary of these datasets is provided in Table 1C.

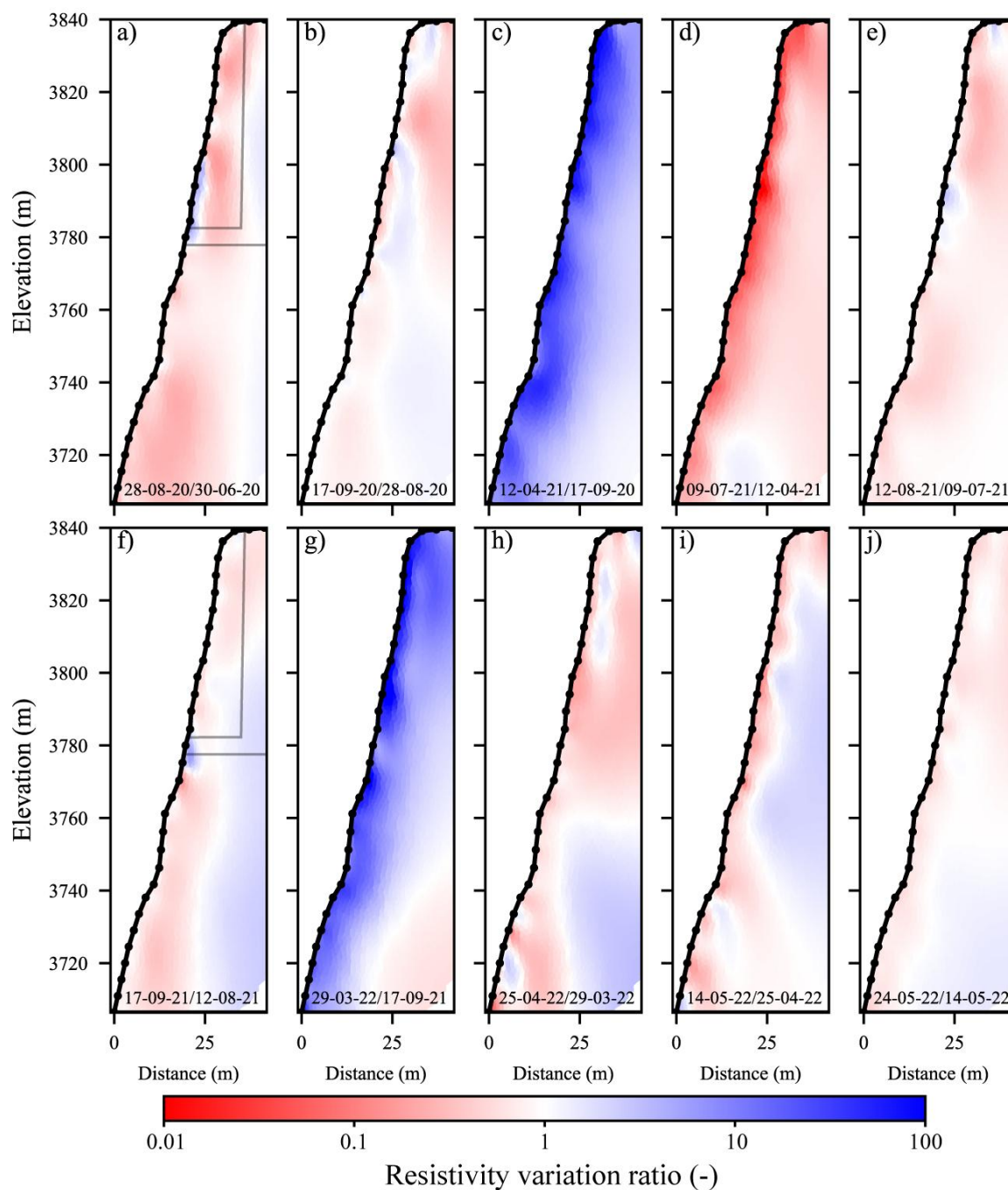


770

771 **Figure D1.** Electrical resistivity tomograms at different dates (from June-2020 to June-2022) along the  
 772 NW side (NW profile). The conductive zone (in warm colors) indicates the approximate position of the  
 773 gallery and elevator (see Fig. 5). The red dots (P1 in panel a) indicate the positions of the thermal sensors  
 774 in the borehole BH-NW. Data presented on Figures 8, 10 and 11 are extracted at the position of the red  
 775 dots (P1 and P2).

776

777



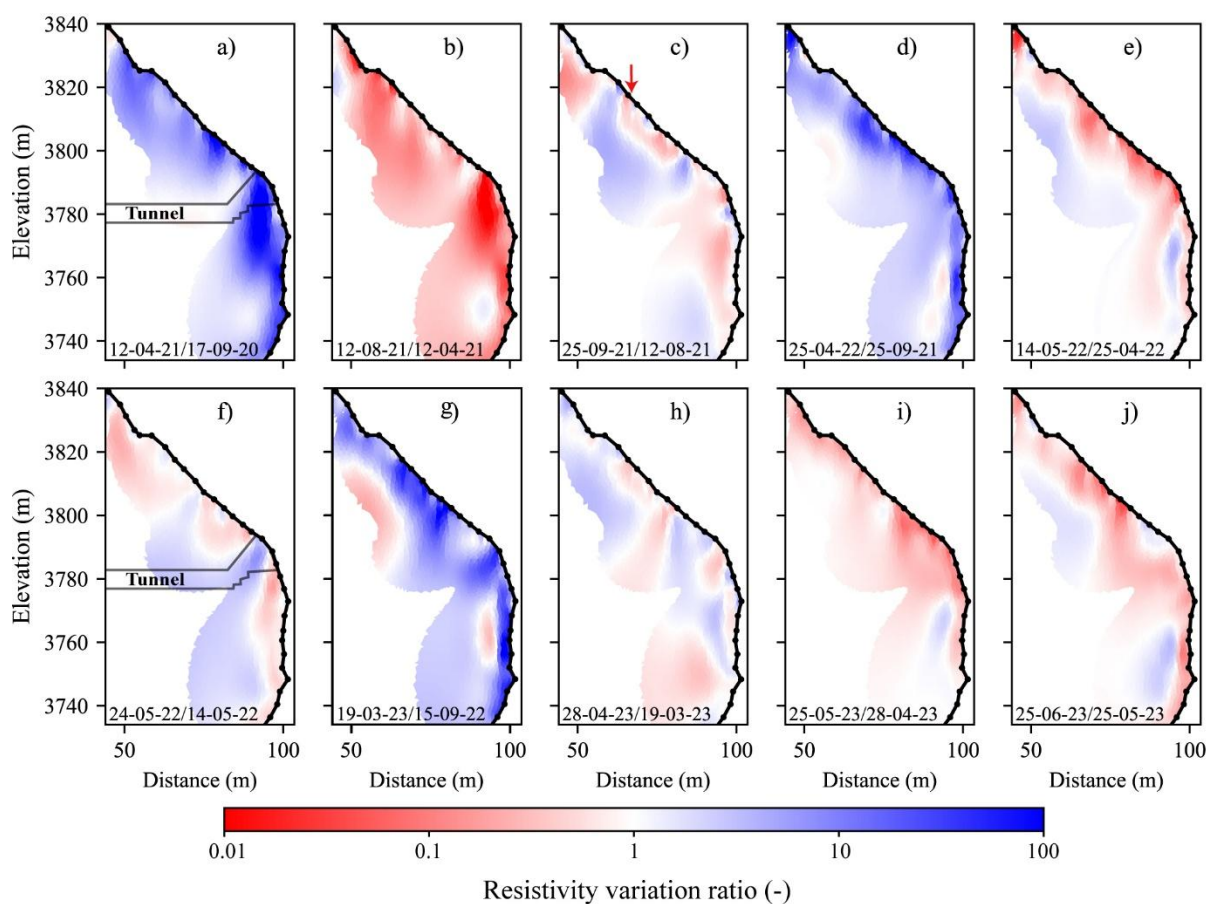
778

779 **Figure D2.** Resistivity variation ratio between consecutive electrical resistivity tomograms (shown in  
 780 Fig. 8) along the NW side. Blue colors indicate an increase in resistivity, while red colors represent a  
 781 decrease in resistivity from one measurement to the next.

782

783 Figure D3 illustrates the resistivity variation ratio between successive measurements on  
 784 the S profile (Figure 13). The dynamics of the active layer are evident, with freezing-thawing  
 785 effects visible near the surface (*e.g.*, Fig. D3a, d, and g). The heat effect (*i.e.*, decrease in

786 resistivity values near the surface) is more pronounced in the lower section (below the gallery).  
 787 Another type of anomaly could be observed at greater depth, where heat and/or cool waves  
 788 resulting of heat transfer (with delay) lead to local variations at greater depth (*e.g.*, Fig. D3, e,  
 789 g and i). In contrast, the fractured zone in the upper portion obscures the temperature  
 790 dependency of resistivity due to fluctuations in air and water content (*i.e.*, resistivity in this zone  
 791 is impacted by factors beyond just temperature). Water infiltration in this area could explain the  
 792 rapid and significant decrease in resistivity observed between 3790 and 3820 m a.s.l. (*e.g.*, Fig.  
 793 D3c, f, and j), which increases the thickness of active layer in this zone.



794  
 795 Figure D3. Resistivity variation ratio between consecutive electrical resistivity tomograms (shown in  
 796 Fig. 13) along the South side. Blue colors indicate an increase in resistivity, while red colors represent  
 797 a decrease in resistivity from one measurement to the next. The red arrow shows the position of  
 798 possible water infiltration inferred from the relative variation compared with the surrounding area.  
 799

800 **References**

- 801 Abdulsamad, F., Revil, A., Ghorbani, A., Toy, V., Kirilova, M., Coperey, A., Duvillard, P. A., Ménard,  
802 G., and Ravel, L.: Complex conductivity of graphitic schists and sandstones. *Journal of*  
803 *Geophysical Research: Solid Earth*, 124, 8223–8249. <https://doi.org/10.1029/2019JB017628>, 2019.
- 804 Ben-Asher, M., Chabas, A., Josnin, J.-Y., Bock, J., Malet, E., Poulain, A., Perrette, Y., and Magnin, F.:  
805 Water flow timing, quantity, and sources in a fractured high mountain permafrost rock wall,  
806 *EGUsphere* [preprint], <https://doi.org/10.5194/egusphere-2025-2450>, 2026.
- 807 Ben-Asher, M., Magnin, F., Westermann, S., Bock, J., Malet, E., Berthet, J., Ravel, L., and Deline,  
808 P.: Estimating surface water availability in high mountain rock slopes using a numerical energy  
809 balance model, *Earth Surf. Dyn.*, 11, 899–915, <https://doi.org/10.5194/esurf-11-899-2023>, 2023.
- 810 Binley, A. and Kemna, A.: DC Resistivity and Induced Polarization Methods, in: *Hydrogeophysics,*  
811 *Water Science and Technology Library book series*, edited by: Rubin, Y. and Hubbard, S.  
812 S., volume 50, 129–156, [https://doi.org/10.1007/1-4020-3102-5\\_5](https://doi.org/10.1007/1-4020-3102-5_5), 2005.
- 813 Bruel, R., Arthaud, F., Magnin, F., Napoleoni, R., Van Reeth, C., Augé, V., Sagot, C., Fructus, M.,  
814 Birck, C., Choler, P., 2026. Different temperature responses of mountain rockwalls, soils, and lakes  
815 to summer heat waves. *Reg Environ Change* 26, 34. <https://doi.org/10.1007/s10113-025-02517-3>
- 816 Campbell, S., Rosa T. Affleck, Sinclair, S.: Ground-penetrating radar studies of permafrost, periglacial,  
817 and near-surface geology at McMurdo Station, Antarctica. *Cold Regions Science and Technology*,  
818 148, Pages 38–49, <https://doi.org/10.1016/j.coldregions.2017.12.008>, 2018.
- 819 Cathala, M., Bock, J., Abdulsamad, F., Deline, P., Josnin, J.-Y., Ravel, L., Revil, A., Richard, J.,  
820 Verroust, F., and Magnin, F.: Assessing the role of permafrost in the preconditioning and triggering  
821 factors of the September 2020 Crête des Grangettes rockfall (southern French Alps),  
822 *Géomorphologie: relief, processus, environnement*, 30, 3, 171–188, <https://doi.org/10.4000/12yqn>,  
823 2024.
- 824 Cimpoiasu, M.O., Kuras, O., Harrison, H., Wilkinson, P. B., Meldrum, P., Chambers, J. E., Liljestrang,  
825 D., Oroza, C., Schmidt, S. K., Sommers, P., Vimercati, L., Irons, T. P., Lyu, Z., Solon, A., and

- 826 Bradley, J. A. (2025). High-resolution 4D electrical resistivity tomography and below-ground point  
827 sensor monitoring of High Arctic deglaciated sediments capture zero-curtain effects, freeze–thaw  
828 transitions, and mid-winter thawing. *The Cryosphere*, 19, 401–421, [https://doi.org/10.5194/tc-19-](https://doi.org/10.5194/tc-19-401-2025)  
829 401-2025.
- 830 Coperey, A., Revil, A., Abdulsamad, F., Stutz, B., Duvillard, P.A., and Ravel, L.: Low frequency  
831 induced polarization of porous media undergoing freezing: preliminary observations and modeling,  
832 *Journal of Geophysical Research: Solid Earth*, 124, doi:10.1029/2018JB017015, 2019.
- 833 Dahlin, T., and Zhou, B.: A numerical comparison of 2D resistivity imaging with 10 electrode arrays,  
834 *Geophys. Prospect.*, 52, 379–398. <https://doi.org/10.1111/j.1365-2478.2004.00423.x>, 2004.
- 835 Doetsch, J., Ingeman-Nielsen, T., Christiansen, A. V., Fiandaca, G., Auken, E., and Elberling, B.: Direct  
836 current (DC) resistivity and induced polarization (IP) monitoring of active layer dynamics at high  
837 temporal resolution, *Cold Reg. Sci. Technol.*, 119, 16–28,  
838 <https://doi.org/10.1016/j.coldregions.2015.07.002>, 2015.
- 839 Draebing, D.: Application of refraction seismics in alpine permafrost studies: A review, *Earth-Science*  
840 *Reviews*, 155, 136–152, <https://doi.org/10.1016/j.earscirev.2016.02.006>, 2016.
- 841 Duvillard, P. A., Revil, A., Qi, Y., Soueid Ahmed, A., Coperey, A., and Ravel, L.: Three-Dimensional  
842 Electrical Conductivity and Induced Polarization Tomography of a Rock Glacier, *J. Geophys. Res.-*  
843 *Sol. Ea.*, 123, 9528–9554, <https://doi.org/10.1029/2018JB015965>, 2018.
- 844 Duvillard, P.A., Magnin, F., Revil, A., Legay, A., Ravel, L., Abdulsamad, F., and Coperey, A.:  
845 Temperature distribution in a permafrost-affected rock ridge from conductivity and induced  
846 polarization tomography, *Geophys. J. Int.*, 225, 1207–1221, <https://doi.org/10.1093/gji/ggaa597>,  
847 2021.
- 848 Edwards, S. L.: A modified pseudosection for resistivity and IP. *Geophysics*, 42, 1020–  
849 1036, <https://doi.org/10.1190/1.1440762>, 1977.
- 850 Etzelmüller, B., Czekirda, J., Magnin, F., Duvillard, P.-A., Ravel, L., Malet, E., Aspaas, A.,  
851 Kristensen, L., Skrede, I., Majala, G. D., Jacobs, B., Leinauer, J., Hauck, C., Hilbich, C., Böhme,  
852 M., Hermanns, R., Eriksen, H. Ø., Lauknes, T. R., Krautblatter, M., and Westermann, S.:

- 853 Permafrost in monitored unstable rock slopes in Norway – new insights from temperature and  
854 surface velocity measurements, geophysical surveying, and ground temperature modelling, *Earth*  
855 *Surf. Dynam.*, 10, 97–129, <https://doi.org/10.5194/esurf-10-97-2022>, 2022.
- 856 Farzamian M, Vieira G, Monteiro Santos FA, et al.: Detailed detection of active layer freeze-thaw  
857 dynamics using quasi-continuous electrical resistivity tomography (Deception Island, Antarctica).  
858 *Cryosphere*.14(3):1105-1120. <https://doi.org/10.5194/tc-14-1105-2020>, 2020.
- 859 Günther, T., Rücker, C., and Spitzer, K.: Three-dimensional modelling and inversion of dc resistivity  
860 data incorporating topography-II. Inversion. *Geophysical Journal International*, Volume 166, Issue  
861 2, August 2006, Pages 506–517, <https://doi.org/10.1111/j.1365-246X.2006.03011.x>, 2006.
- 862 Hartmeyer, I., Delleske, R., Keuschnig, M., Krautblatter, M., Lang, A., Schrott, L., and Otto, J.-C.:  
863 Current glacier recession causes significant rockfall increase: the immediate paraglacial response  
864 of deglaciating cirque walls, *Earth Surf. Dynam.*, 8, 729–751, [https://doi.org/10.5194/esurf-8-729-](https://doi.org/10.5194/esurf-8-729-2020)  
865 2020, 2020.
- 866 Hasler, A., Gruber, S., Font, M., and Dubois, A.: Advective Heat Transport in Frozen Rock Clefts:  
867 Conceptual Model, Laboratory Experiments and Numerical Simulation, *Permafrost and Periglacial*  
868 *Processes*, 22, 378–389, <https://doi.org/10.1002/ppp.737>, 2011.
- 869 Hauck, C., Böttcher, M., and Maurer, H.: A new model for estimating subsurface ice content based on  
870 combined electrical and seismic data sets, *The Cryosphere*, 5, 453–468, [https://doi.org/10.5194/tc-](https://doi.org/10.5194/tc-5-453-2011)  
871 5-453-2011, 2011.
- 872 Hauck, C., and Hilbich C.: Preconditioning of mountain permafrost towards degradation detected by  
873 electrical resistivity. *Environ. Res. Lett.* 19 064010. <https://doi.org/10.1088/1748-9326/ad3c55>,  
874 2024.
- 875 Herring, T., Lewkowicz, A. G., Hauck, C., Hilbich, C., Mollaret, C., Oldenborger, G. A., Uhlemann, S.,  
876 Farzamian, M., Calmels, F., and Scandroglio, R.: Best practices for using electrical resistivity  
877 tomography to investigate permafrost, *Permafrost Periglac.*, 34, 494–512,  
878 <https://doi.org/10.1002/ppp.2207>, 2023.

- 879 Hilbich, C., Marescot, L., Hauck, C., Loke, M. H., and Mäusbacher, R.: Applicability of Electrical  
880 Resistivity Tomography Monitoring to Coarse Blocky and Ice-rich Permafrost Landforms,  
881 Permafrost Periglac., 20, 269–284, <https://doi.org/10.1002/ppp.652>, 2009.
- 882 Hilbich, C., Hauck, C., Hoelzle, M., Scherler, M., Schudel, L., Völksch, I., Vonder Mühl, D., and  
883 Mäusbacher, R.: Monitoring Mountain permafrost evolution using electrical resistivity  
884 tomography: A 7-year study of seasonal, annual, and long-term variations at Schilthorn, Swiss  
885 Alps, *J. Geophys. Res.-Earth*, 113, F01S90, <https://doi.org/10.1029/2007JF000799>, 2008.
- 886 Jacquemart, M., Weber, S., Chiarle, M., Chmiel, M., Cicoira, A., Corona, C., Eckert, N., Gaume, J.,  
887 Giacona, F., Hirschberg, J., Kaitna, R., Magnin, F., Mayer, S., Moos, C., van Herwijnen, A., and  
888 Stoffel, M.: Detecting the impact of climate change on alpine mass movements in observational  
889 records from the European Alps, *Earth-Science Reviews*, 258, 104886,  
890 <https://doi.org/10.1016/j.earscirev.2024.104886>, 2024.
- 891 Karaoulis, M., Tsourlos, P., Kim, J., and Revil, A.: 4D time-lapse ERT inversion: introducing combined  
892 time and space constraints, *Near Surf. Geophys.*, 12, 25–34, [https://doi.org/10.3997/1873-](https://doi.org/10.3997/1873-0604.2013004)  
893 [0604.2013004](https://doi.org/10.3997/1873-0604.2013004), 2013.
- 894 Keuschnig, M., Krautblatter, M., Hartmeyer, I., Fuss, C. and Schrott, L.: Automated electrical resistivity  
895 tomography testing for early warning in unstable permafrost rock walls around Alpine  
896 infrastructure, *Permafrost Periglac.*, 28, 158–171. <https://doi.org/10.1002/ppp.1916>, 2017.
- 897 Krautblatter, M. and Hauck, C.: Electrical resistivity tomography monitoring of permafrost in solid rock  
898 walls, *J. Geophys. Res.*, 112, F02S20, <https://doi.org/10.1029/2006JF000546>, 2007.
- 899 Krautblatter M, Verleysdonk S, Flores-Orozco A., and Kemna A.: Temperature-calibrated imaging of  
900 seasonal changes in permafrost rock walls by quantitative electrical resistivity tomography  
901 (Zugspitze, German/Austrian Alps). *J. Geophys. Res.*, 115, F02003,  
902 <https://doi.org/10.1029/2008JF001209>, 2010.
- 903 Krautblatter, M., Funk, D. and Günzel, F.K.: Why permafrost rocks become unstable: a rock–ice-  
904 mechanical model in time and space. *Earth Surf. Process. Landforms*, 38, 876–887.  
905 <https://doi.org/10.1002/esp.3374>, 2013.

- 906 Loke, M. H.: Time-lapse resistivity imaging inversion, paper presented at 5th Meeting of the  
907 Environmental and Engineering Society European Section, Budapest. 1999.
- 908 Magnin, F., Deline, P., Ravanel, L., Noetzli, J., and Pogliotti, P.: Thermal characteristics of permafrost  
909 in the steep alpine rock walls of the Aiguille du Midi (Mont Blanc Massif, 3842 m a.s.l), *The*  
910 *Cryosphere*, 9, 109–121, <https://doi.org/10.5194/tc-9-109-2015>, 2015b.
- 911 Magnin, F., Krautblatter, M., Deline, P., Ravanel, L., Malet, E. and Bevington, A.: Determination of  
912 warm, sensitive permafrost areas in near-vertical rockwalls and evaluation of distributed models by  
913 electrical resistivity tomography, *J. geophys. Res.-Earth*, 120, 745–762,  
914 <https://doi.org/10.1002/2014JF003351>, 2015a.
- 915 Magnin, F., Ravanel, L., Bodin, X., Deline, P., Malet, E., Krysiecki, J.-M., et al.: Main results of  
916 permafrost monitoring in the French Alps through the PermaFrance network over the period 2010–  
917 2022. *Permafrost and Periglacial Processes*, 35(1), 3–23. <https://doi.org/10.1002/ppp.2209>, 2024
- 918 Magnin, F. and Josnin, J.-Y. Water flows in Rock Wall permafrost: a numerical approach coupling  
919 hydrological and thermal processes. *Journal of Geophysical Research - Earth Surface*, 126(11),  
920 e2021JF006394. <https://doi.org/10.1029/2021JF006394>, 2021.
- 921 Magnin, F., Josnin, J.-Y., Ravanel, L., Pergaud, J., Pohl, B., and Deline, P.: Modelling rock wall  
922 permafrost degradation in the Mont Blanc massif from the LIA to the end of the 21st century, *The*  
923 *Cryosphere*, 11, 1813–1834, <https://doi.org/10.5194/tc-11-1813-2017>, 2017.
- 924 Maierhofer, T., Flores Orozco, A., Roser, N., Limbrock, J. K., Hilbich, C., Moser, C., Kemna, A., Drigo,  
925 E., Morra di Cella, U., and Hauck, C.: Spectral induced polarization imaging to monitor seasonal  
926 and annual dynamics of frozen ground at a mountain permafrost site in the Italian Alps, *The*  
927 *Cryosphere*, 18, 3383–3414, <https://doi.org/10.5194/tc-18-3383-2024>, 2024.
- 928 Mewes, B., Hilbich, C., Delaloye, R., and Hauck, C.: Resolution capacity of geophysical monitoring  
929 regarding permafrost degradation induced by hydrological processes, *The Cryosphere*, 11, 2957–  
930 2974, <https://doi.org/10.5194/tc-11-2957-2017>, 2017.
- 931 Mollaret, C., Wagner, F. M., Hilbich, C., Scapozza, C., and Hauck, C.: Petrophysical Joint Inversion  
932 Applied to Alpine Permafrost Field Sites to Image Subsurface Ice, Water, Air, and Rock Contents,  
933 *Front. Earth Sci.*, 8, 1–25, <https://doi.org/10.3389/feart.2020.00085>, 2020.

- 934 Mollaret, C., Hilbich, C., Pellet, C., Flores-Orozco, A., Delaloye, R., and Hauck, C.: Mountain  
935 permafrost degradation documented through a network of permanent electrical resistivity  
936 tomography sites, *The Cryosphere*, 13, 2557–2578, <https://doi.org/10.5194/tc-13-2557-2019>, 2019.
- 937 Noetzli J., Gruber S., Kohl T., Salzmann N., Haeberli W.: Three-dimensional distribution and evolution  
938 of permafrost temperatures in idealized high-mountain topography. *Journal of Geophysical*  
939 *Research: Earth Surface* 112, n/a–n/a. <https://doi.org/10.1029/2006JF000545>, 2007.
- 940 Noetzli, J., Isaksen, K., Barnett, J. et al.: Enhanced warming of European mountain permafrost in the  
941 early 21st century. *Nat Commun* 15, 10508. <https://doi.org/10.1038/s41467-024-54831-9>, 2024
- 942 Moser, C., Morra di Cella, U., Hauck, C., and Flores Orozco, A.: Spectral induced polarization survey  
943 for the estimation of hydrogeological parameters in an active rock glacier, *The Cryosphere*, 19,  
944 143–171, <https://doi.org/10.5194/tc-19-143-2025>, 2025.
- 945 Offer, M., Weber, S., Krautblatter, M., Hartmeyer, I., and Keuschnig, M.: Pressurised water flow in  
946 fractured permafrost rocks revealed by borehole temperature, electrical resistivity tomography, and  
947 piezometric pressure, *The Cryosphere*, 19, 485–506, <https://doi.org/10.5194/tc-19-485-2025>, 2025.
- 948 Pavoni, M., Boaga, J., Wagner, F. M., Bast, A., Phillips, M.: Characterization of rock glaciers  
949 environments combining structurally-coupled and petrophysically-coupled joint inversions of  
950 electrical resistivity and seismic refraction datasets, *Journal of Applied Geophysics*, 215, 0926-  
951 9851, <https://doi.org/10.1016/j.jappgeo.2023.105097>, 2023.
- 952 Piolat, L., Revil, A., Richard, J., Ghorbani G., Cosme, P., Géraud, Y., Casotti, C., Vaudelet, P., Diraison,  
953 M., and Favier, A.: Induced polarization of volcanic rocks. 8. The case of intrusive igneous  
954 rocks, *Geophysical Journal International*, Volume 241, Issue 2, Pages 1348  
955 1372, <https://doi.org/10.1093/gji/ggaf102>, 2025.
- 956 Ravanel, L., Magnin, F. and Deline, P.: Impacts of the 2003 and 2015 summer heatwaves on permafrost-  
957 affected rock-walls in the Mont Blanc massif. *Science of the Total Environment*, 609, 132–143.  
958 <https://doi.org/10.1016/j.scitotenv.2017.07.055>, 2017.
- 959 Revil, A., Cathles, L. M., Losh, S., & Nunn, J. A.: Electrical conductivity in shaly sands with  
960 geophysical applications. *Journal of Geophysical Research*, 103(B10), 23,925–23,936.  
961 <https://doi.org/10.1029/98JB02125>, 1998.

- 962 Revil, A., Ghorbani, A., Zhao, X., Mouyeaux, A., Barrère, L., Richard, J., Peyras, L., and Vaudelet, P.  
963 Groundwater flow paths using combined self-potential, electrical resistivity, and induced  
964 polarization signals, *Geophysical Journal International*, 239, 2, 798–  
965 820, <https://doi.org/10.1093/gji/ggae291>, 2024.
- 966 Revil, A., Coperey, A., Mao, D., Abdulsamad, F., Ghorbani, A., Rossi, M., and Gasquet, D. Induced  
967 polarization response of porous media with metallic particles — Part 8: Influence of temperature  
968 and salinity: *Geophysics*, 83, no. 6, E435–E456, <https://doi.org/10.1190/geo2018-0089.1>, 2018.
- 969 Revil A., J. Richard, A. Ghorbani, F. Magnin, P.A. Duvillard, M. Marcer, F. Abdulsamad, T. Ingeman-  
970 Nielsen, L. Ravel, C. Lambiel, X. Bodin, H. Cai, X. Hu, and P Vaudelet,: Induced polarization  
971 as a tool to characterize permafrost 1. Theory and laboratory experiments, *Geophysical Journal*  
972 *International*, 244, 1. <https://doi.org/10.1093/gji/ggaf443>, 2026a.
- 973 Revil A., P. A. Duvillard, M. Marcer, J. Richard, T. Ingeman-Nielsen, F. Abdulsamad, F. Magnin, B.  
974 Charonnat, H. Cai, X. Hu, L. Ravel, and P. Schoeneich: Induced polarization as a tool to  
975 characterize permafrost. 2. Applications to low and high-porosity environments, *Geophysical*  
976 *Journal International*, 244, 1. <https://doi.org/10.1093/gji/ggaf464>, 2026b.
- 977 Rucker, C., Günther, T., and Wagner, F. M.: pyGIMLi: An open-source library for modelling and  
978 inversion in geophysics, *Computers & Geosciences*, 109, 106–123,  
979 <https://doi.org/10.1016/j.cageo.2017.07.011>, 2017.
- 980 Sass, O.: Rock Moisture Fluctuations During Freeze-thaw Cycles: Preliminary Results from Electrical  
981 Resistivity Measurements, *Polar Geogr.*, 28, 13–31, <https://doi.org/10.1080/789610157>, 2004.
- 982 Scandroglio, R., Draebing, D., Offer, M., Krautblatter, M.: 4D quantification of alpine permafrost  
983 degradation in steep rock walls using a laboratory-calibrated electrical resistivity tomography  
984 approach, *Near Surface Geophys.*, 19, 241-260, <https://doi.org/10.1002/nsg.12149>, 2021.
- 985 Smith, S.L., O'Neill, H.B., Isaksen, K. et al. The changing thermal state of permafrost. *Nat Rev Earth*  
986 *Environ* 3, 10–23 (2022). <https://doi.org/10.1038/s43017-021-00240-1>
- 987 Steiner, M., Wagner, F. M., and Flores Orozco, A.: Improved characterization of alpine permafrost  
988 through structurally constrained inversion of refraction seismic data, *The Cryosphere Discuss*,  
989 <https://doi.org/10.5194/tc-2019-52>, 2019.

- 990 Steiner, M., Wagner, F. M., Maierhofer, T., Schöner, W., and Flores Orozco, A. Improved estimation  
991 of ice and water contents in alpine permafrost through constrained petrophysical joint inversion:  
992 The Hoher Sonnblick case study," *GEOPHYSICS* 86: WB61-WB75.  
993 <https://doi.org/10.1190/geo2020-0592.1>, 2021.
- 994 Wagner, F. M., Mollaret, C., Kemna, A., and Hauck, C.: Quantitative imaging of water, ice and air in  
995 permafrost systems through petrophysical joint inversion of seismic refraction and electrical  
996 resistivity data, *Geophys. J. Int.*, 219, 1866–1875, <https://doi.org/10.1093/gji/ggz402>, 2019.
- 997 Zimmermann, E., Kemna, A., Berwix, J., Glaas, W., Münch, H. M., and Huisman, J. A. A high accuracy  
998 impedance spectrometer for measuring sediments with low polarizability. *Measurement Science*  
999 *and Technology*, 19(10), 105603. <https://doi.org/10.1088/0957-0233/19/10/105603>, 2008.